FEATURE ARTICLE

Transmission Electron Microscopy of Shape-Controlled Nanocrystals and Their Assemblies

Z. L. Wang*

School of Materials Science and Engineering, Georgia Institute of Technology, Atlanta, Georgia 30332-0245

Received: October 7, 1999; In Final Form: November 18, 1999

The physical and chemical properties of nanophase materials rely on their crystal and surface structures. Transmission electron microscopy (TEM) is a powerful and unique technique for structure characterization. The most important application of TEM is the atomic-resolution real-space imaging of nanoparticles. This article introduces the fundamentals of TEM and its applications in structural determination of shape-controlled nanocrystals and their assemblies. By forming a nanometer size electron probe, TEM is unique in identifying and quantifying the chemical and electronic structure of individual nanocrystals. Electron energy-loss spectroscopy analysis of the solid-state effects and mapping the valence states are even more attractive. In situ TEM is demonstrated for characterizing and measuring the thermodynamic, electric, and mechanical properties of individual nanostructures, from which the structure−property relationship can be registered with a specific nanoparticle/structure.

1. Structure of Nanocrystals and Physical Chemistry

The unique chemical and physical properties of nanocrystals are determined not only by the large portion of surface atoms but also by the crystallographic structures of the particle surface. The former is determined by the size of the particles, and the latter relies on the particle shape. A large amount of research has been carried out to investigate the effects of particle size on their properties. One typical example is that the melting temperature of nanocrystals strongly depends on the crystal size and is substantially lower than the bulk melting temperature. The melting point of Au particles of core size 2.5 nm is ∼40% lower than that of bulk gold.[1] Similar behavior has been observed for sodium clusters[2] and CdS nanocrystals.[3] The other interesting property is the quantum confinement effect in small size metallic and semiconductor quantum dots.[4,5] The shift of electron energy levels as a function of particle size gives rise of emission of photons with unique wavelengths, potentially useful for optoelectronics.

The particle shapes are closely related to the crystallographic surfaces that enclose the particles. The {111}, {100}, and possibly {110} surfaces of face-centered cubic structured metal particles, for example, are different not only in the surface atom densities but also the electronic structure, bonding, and possibly chemical reactivities. The sublimation activation energy of Au {110} faces, for example, has been found to be significantly lower than that of {100} and {111}, resulting in the sublimation of Au atoms from the surface at temperatures as low as 220 °C, much lower than the melting point of bulk gold of 1063 °C.[6] The tetrahedral Pt nanocrystals enclosed mainly by {111} facets have been found to be more stable than the {100} enclosed cubic Pt nanocrystals simply because of the difference in surface energies.[7] Molecular dynamics calculation reveals that the melting process of Au clusters is punctuated by solid-to-solid structural transformations from the low-temperature optimal structures (such as truncated octahedron and truncated decahedron) to icosahedral structures, which are believed to be the intrinsic thermodynamic precursors to the melting transition.[8]

Crystal structures can be determined by X-ray and neutron diffraction, while transmission electron microscopy (TEM) is indispensable for characterization of nanocrystal materials, particularly when particle shape is important. Although scanning tunneling microscopy and atomic force microscopy can provide atomic-resolution images of large crystal surfaces, they are unlikely to clearly resolve the atomic lattices of nanoparticles because of the surface coating and the wobbling of the nanocrystals under the scanning tip. TEM is likely to be very powerful for revealing the atom distributions on nanocrystal surfaces even when they are passivated with polymers. Today's TEM is a versatile tool that provides not only atomic-resolution lattice images but also chemical information at a spatial resolution of 1 nm or better, allowing direct identification the chemistry of a single nanocrystal.[9−12] With a finely focused electron probe, the structural characteristics of a single nanoparticle can be fully characterized. TEM is unique for characterizing the in situ structural evolution of nanocrystals resulting from annealing, electric field, or mechanical stress, such as imaging a single carbon nanotube when a mechanical or electrical measurement is being carried out in situ.[13]

Much of the research in the literature has been focused on the size effect. We have been interested in the property of shape-controlled nanocrystals, aiming at exploring the unique catalysis properties of different crystal faces.[14] The research involves three critical steps: synthesis of shape-controlled nanocrystals, structural characterization, and property characterization. TEM has played a major role in characterizing the shape-controlled nanocrystals. As a review of the research field, this article focuses on the fundamentals of TEM and its applications in characterizing the structure of shape-controlled nanocrystals. The

* Corresponding author. E-mail: zhong.wang@mse.gatech.edu.

10.1021/jp993593c CCC: $19.00
Published on Web 01/11/2000

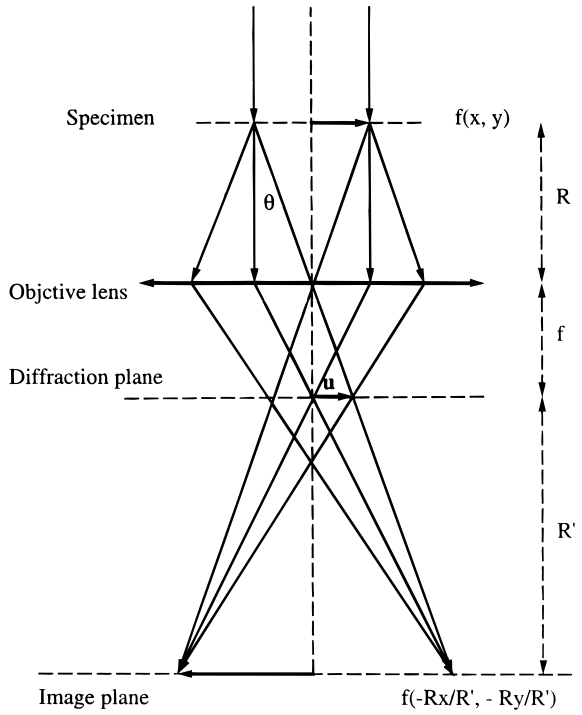

Figure 1. Abbe's theory of image formation in a one-lens transmission electron microscope. This theory is for a general optical system in TEM.

physical basis of atomic scale imaging using TEM will be illustrated first. Then, the applications of TEM for determination of the particle shape and surface structures will be given. In situ structural characterization by TEM will be illustrated. The analysis of nanocrystal self-assembled arrays and the role played by particle shapes in the assembly will be demonstrated. Finally, the investigation of nanocrystal chemical and electronic properties by electron energy-loss spectroscopy will be reviewed.

2. High-Resolution Transmission Electron Microscopy

A modern TEM is composed of an illumination system, a specimen stage, an objective lens system, the magnification system, the data recording system(s), and the chemical analysis system. The electron gun is the heart of the illumination system, which typically uses LaB_6 thermionic emission source or a field emission source. The LaB_6 gun gives a high illumination current, but the current density and the beam coherence are not as high as those of a field emission source. Field emission source is unique for performing high coherence lattice imaging, electron holography, and high spatial resolution microanalysis. The illumination system also includes the condenser lenses that are vitally important for forming a fine electron probe. The specimen stage is key to carrying out structure analysis, because it can be used to perform in situ observations of phenomena induced by annealing, electric field, or mechanical stress, giving the possibility of characterizing the physical properties of individual nanostructures. The objective lens is the heart of a TEM which determines the limit of image resolution. The magnification system consists of intermediate lenses and projection lenses, and it gives a magnification up to 1.5 million. The data recording system tends to be digital with the use of a charge coupled device (CCD), allowing quantitative data processing and quantification. Finally, the chemical analysis system is the energy-dispersive X-ray spectroscopy (EDS) and electron energy loss spectroscopy (EELS), both can be used complementary to quantify the chemical composition of the specimen. EDS relies on the counting of X-rays emitted from the beam-illuminated specimen region as a function of the photon energy, and it is

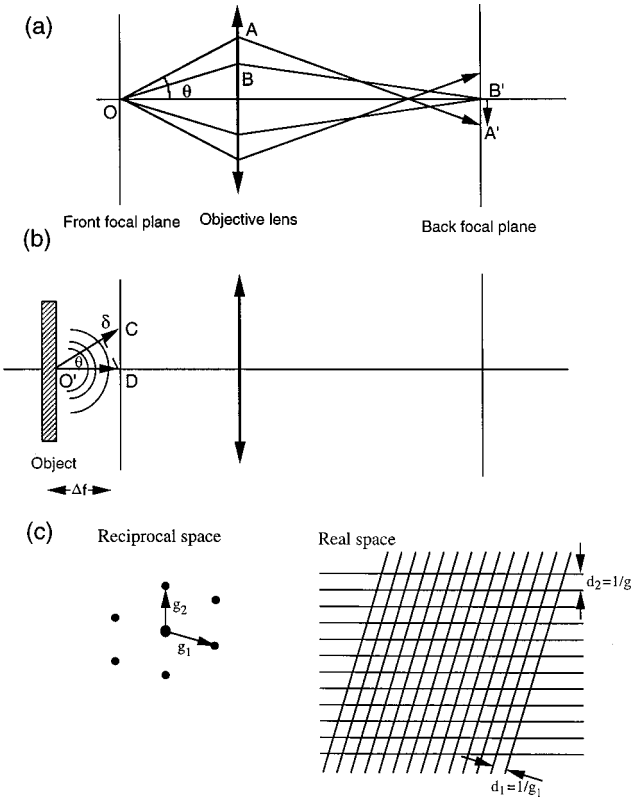

Figure 2. Schematic diagrams showing the phase shift introduced by (a) spherical aberration and (b) objective lens defocus on the electrons scattered off the central optical axis. This nonlinear information transfer characteristics of the TEM gives rise the complexity in interpretation of TEM images. (c) The relationship between the diffraction beams in reciprocal space and the interference lattice fringes in real space (image). The phases of the reflected Bragg beams are modulated by the lens, thus, the image contrast strongly depends on the defocus.

probably the most precise microanalysis technique in TEM. EELS analyzes the intensity distribution of the transmitted electrons as a function of their energy loss. It provides not only the chemical information on the specimen but also its electronic structure. A complementary application of the diffraction, imaging, and spectroscopy techniques available in a TEM is likely to give a more precise and reliable determination of the crystal structure.

2.1. Image Formation. As a start, we first illustrate the image formation process in an TEM. For easy illustration, a TEM is simplified into a single lens microscope, as given in Figure 1, in which only a single objective lens is considered for imaging and the intermediate lenses and projection lenses are omitted. This is because the resolution of the TEM is mainly determined by the objective lens. The entrance surface of a thin foil specimen is illuminated by a parallel or nearly parallel electron beam. The electron beam is diffracted by the lattices of the crystal, forming the Bragg beams which are propagating along different directions. The electron−specimen interaction results in phase and amplitude changes in the electron wave that are determined by quantum mechanical diffraction theory. For a thin specimen and high-energy electrons, the transmitted wave function $\Psi(x,y)$ at the exit face of the specimen can be assumed to be composed of a forward-scattered wave. The exit wave $\Psi(x,y)$ contains the full structural information on the specimen. Unfortunately, this wave will be transmitted nonlinearly by the optic system.

The nonnear-axis propagation of the electrons through the objective lens is the main source of nonlinear information

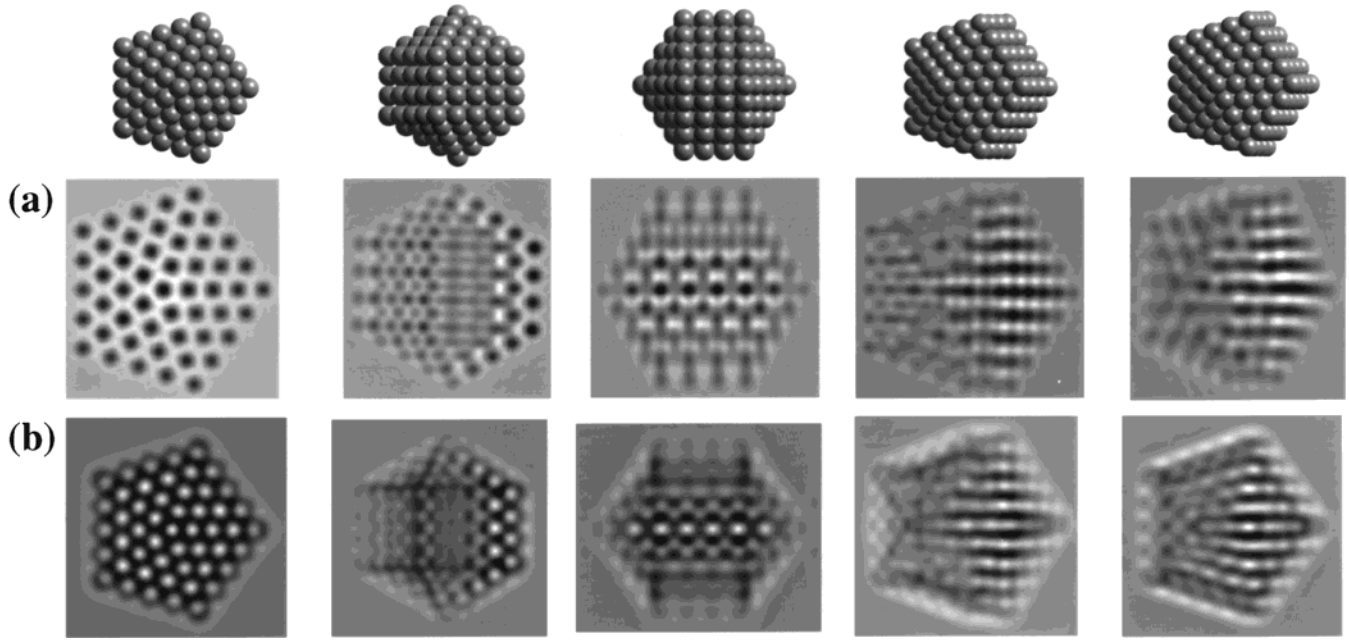

Figure 3. Theoretically simulated images for a decahedral Au particle at various orientations and at focuses of (A) $\Delta f = 42$ nm and (B) $\Delta f = 70$ nm, illustrating the contrast reversal in the two cases (Courtesy of Drs. Ascencio and M. José-Yacamán).

transfer in TEM. The diffracted beams will be focused in the back focal plane, where an objective aperture could be applied. An ideal thin lens brings the parallel transmitted waves to a focus on the axis in the back focal plane. Waves leaving the specimen in the same direction (or angle θ with the optic axis) are brought together at a point on the back focal plane, forming a diffraction pattern. The electrons scattered to angle θ experience a phase shift introduced by the spherical aberration and the defocus of the lens, and this phase shift is a function of the scattering angle. The phase shift due to spherical aberration is caused by a change in focal length as a function of the electron scattering angle, and the phase shift owing to defocus is caused by the spherical characteristics of the emitted wave in free space (e.g., the Huygens principle). The electron wave in real space is related to that in reciprocal space by a Fourier transform for the case of Fraunhofer diffraction. If $\psi(\mathbf{u})$ is the Fourier transform (FT) of the wave $\Psi(\mathbf{r})$ at the exit face of the specimen, the diffraction amplitude function at the back focal plane (diffraction plane) is

$$\psi'(\mathbf{u}) = \psi(\mathbf{u}) \exp[i\chi(\mathbf{u})] \quad (1)$$

where $\mathbf{u}$ is the reciprocal space vector that is related to the scattering angle by $u = 2 \sin \theta/\lambda$, and $\chi(\mathbf{u})$ is the phase function introduced by the objective lens, which is determined by the spherical aberration coefficient C_s of the objective lens and the lens defocus Δf,

$$\chi(\mathbf{u}) = \frac{\pi}{2} C_s \lambda^3 u^4 - \pi \Delta f \lambda u^2 \quad (2)$$

where λ is the electron wavelength. The aberration and defocus of the lens is to modulate the phases of the Bragg beams distributed in reciprocal space. The phase shift introduced by spherical aberration is due to the variation in focal length as a function of the electron scattering angle, resulting in a path length difference (Figure 2a). The ray OA scattered to higher angle will be focused at a shorter focal length in comparison to the OB ray scattered to a lower angle; thus, an imaging broadening will be observed in the back focal plane. The phase factor introduced by defocus represents the relative phase shift of the electrons scattered to an angle θ owing to the increased path length (Figure 2b). From the Huygens' principle, the spherical wave emitted from point O′ to point C and D will have a path length difference of $\delta = \Delta f(1 - \cos \theta)/\cos \theta \approx \Delta f \theta^2/2$. The correspondence phase shift increases as the scattering angle increases.

A high-resolution TEM image of a crystalline specimen is formed by the interference of the Bragg reflected beams (Figure 2c). Since the phase of each Bragg beam is perturbed by the phase shift induced by spherical and defocus, the object information will be transmitted nonlinearly. Mathematically, the wave observed in the front focal plane is the inverse Fourier transform (FT^{-1}) of $\psi'(\mathbf{u})$, and the observed image intensity is

$$I(x,y) = |FT^{-1}[\psi'(\mathbf{u})]|^2 = |\Psi(x,y) \otimes t_{obj}(x,y,\Delta f)|^2 \quad (3)$$

where $\otimes$ indicates a convolution calculation of (x,y), $t_{obj}(x,y,\Delta f)$ is the inverse Fourier transform of the phase function $\exp[i\chi(\mathbf{u})]$. The convolution of the lens transfer function introduces the nonlinear information transfer characteristics of the objective lens, leading to complexity in image interpretation. Equation 3 is the Abbe's imaging theory which correlates the object wave function $\Psi(x,y)$ with the experimentally observed image intensity distribution $I(x,y)$. It is easier to work from $\Psi(x,y)$ to $I(x,y)$, but not vice versa.

2.2. Contrast Mechanisms. Images in TEM are usually dominated by three types of contrast. The first is diffraction contrast, which is produced due to the perturbation of local strain/defects/dislocation on the intensities of the Bragg reflected beams.[15] This contrast emphasizes the effect of defects on the amplitude of the transmitted wave, and it is also called amplitude contrast. If the image is formed by selecting the central transmitted wave only, the image contrast is most sensitive to defect structures and the image resolution is limited to ~2 nm. For nanocrystals, most of the grains are defect-free in volume, while a high density of defects are localized at the surface or grain boundary, diffraction contrast can be useful for capturing strain distribution in nanocrystals of sizes larger than 15 nm.

Second, phase contrast is produced by the phase modulation of the incident electron wave when it transmits through the

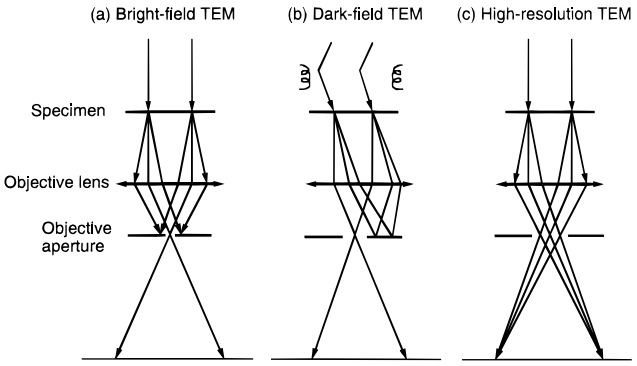

Figure 4. Optic ray diagrams for performing (a) bright-field, (b) dark-field, and (c) high-resolution imaging in an TEM.

crystal potential. This type of contrast is sensitive to the atom distribution in the specimen. To illustrate the physics of phase contrast, we consider the modulation of a crystal potential to the electron wavelength. From the de Brogli relation, the wavelength λ of an electron is related to its momentum, p, by

$$\lambda = \frac{h}{p} \tag{4}$$

When the electron goes through a crystal potential field, its kinetic energy is perturbed by the variation of the potential field, resulting in a phase shift with respect to the electron wave that travels in a space free of potential field. For a specimen of thickness, d, the phase shift is

$$\Psi \approx \sigma V_p(x,y) = \sigma \int_0^d \mathrm{d}z\, V(x,y,z) \tag{5}$$

where $\sigma = \pi/\lambda U_0$, U_0 is the acceleration voltage, and $V_p(x,y)$ the thickness-projected potential of the crystal. Equation 5 clearly shows that the phase contrast image is the result of the thickness-projected image along the beam direction (z-axis) of a three-dimensional object. The 3-D shape of the crystal can be revealed using the images recorded at least from two independent orientations.

Electron transmission through a thin crystal can be characterized by a phase modulation function, which is known to be the *phase object approximation* (POA). This approximation assumes that the electron wave is modulated only in phase but not in amplitude (e.g., phase contrast). Therefore, the electron wave at the exit face of a thin crystal is approximated to be

$$\Psi(x,y) = \exp[i\sigma V_p(x,y)] \tag{6}$$

If the incident beam travels along a low-index zone axis, the variation of $V_p(x,y)$ across atom rows is a sharp varying function because an atom can be approximated by a narrow potential well and its width is on the order of 0.2−0.3 Å. This sharp phase variation is the basis of phase contrast, the fundamental of atomic-resolution imaging in TEM.

The last one is mass thickness or atomic number contrast. Atoms with different atomic numbers exhibit different powers of scattering. If the image is formed by collecting the electrons scattered to high angles, the image contrast would be sensitive to the average atomic number along the beam direction. This type of imaging is most frequently performed in scanning transmission electron microscopy.

2.3. The White and Dark Spots in the Image, Which Represent Atoms? In a high-resolution TEM (HRTEM) image, one usually wonders if the atoms are dark or bright. To answer this question, one must examine the imaging conditions. For the clarity of the following discussion, the weak scattering object approximation (WPOA) is made. If the specimen is so thin that the projected potential satisfies $|\sigma V_p| \ll 1$, the phase grating function in eq 6 is approximated by

$$\Psi(x,y) \approx 1 + i\sigma V_p(x,y) \tag{7}$$

From the imaging theory presented in eq 3, and ignoring the σ^2 term, the image intensity is calculated by

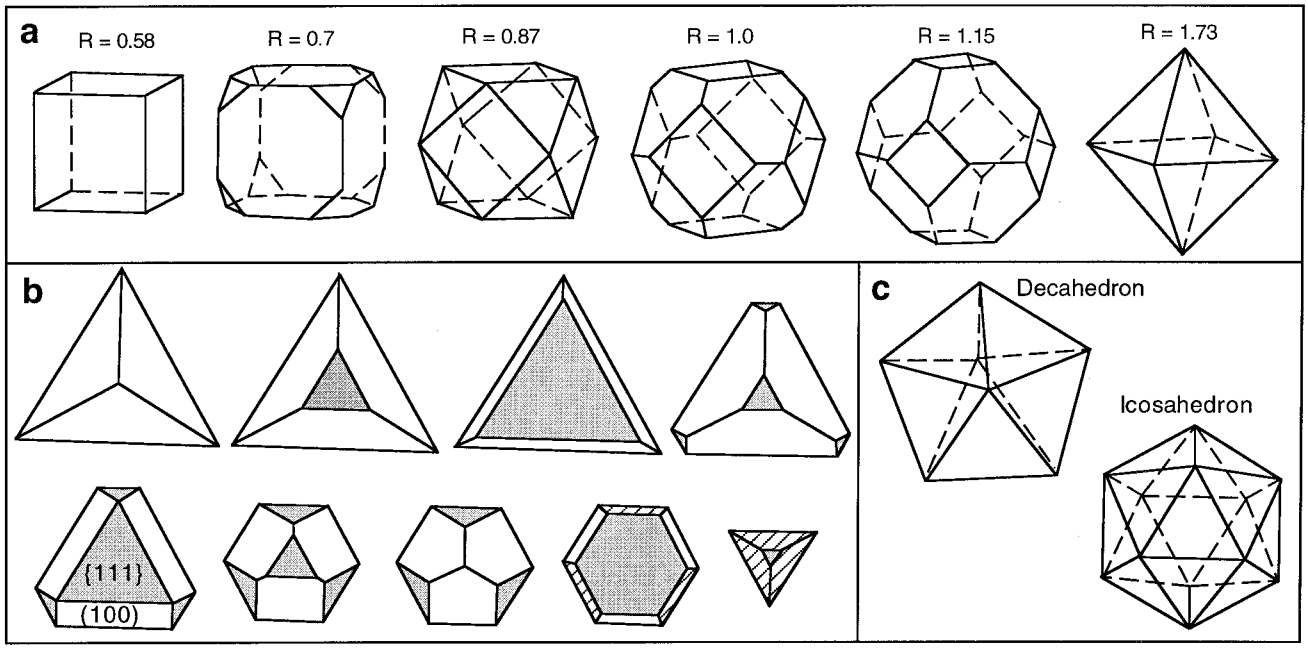

Figure 5. (a) Geometrical shapes of cubooctahedral nanocrystals as a function of the ratio, R, of the growth rate along the ⟨100⟩ to that of the ⟨111⟩. (b) Evolution in shapes of a series of (111) based nanoparticles as the ratio of {111} to {100} increases. The beginning particle is bounded by three {100} facets and a (111) base, while the final one is a {111} bounded tetrahedron. (c) Geometrical shapes of multiply twinned decahedral and icosahedral particles.

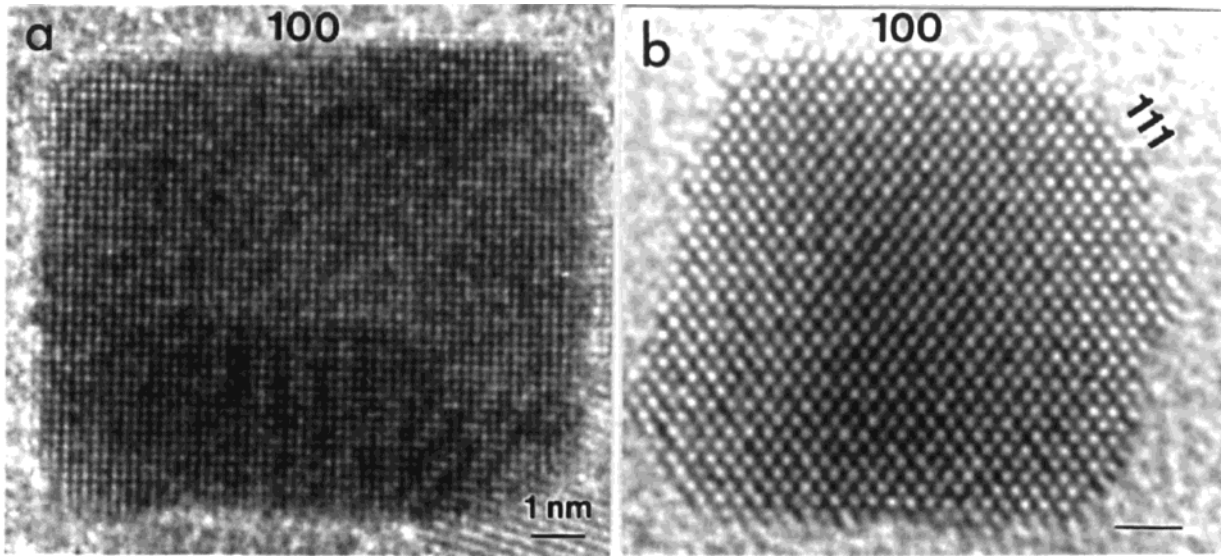

Figure 6. HRTEM images of cubic Pt nanocrystals oriented along (a) [001] and (b) [110], showing surface steps/ledges and the thermodynamically inequilibrium shapes (The Pt nanocrystals were supplied by Prof. M. A. El-Sayed's group).

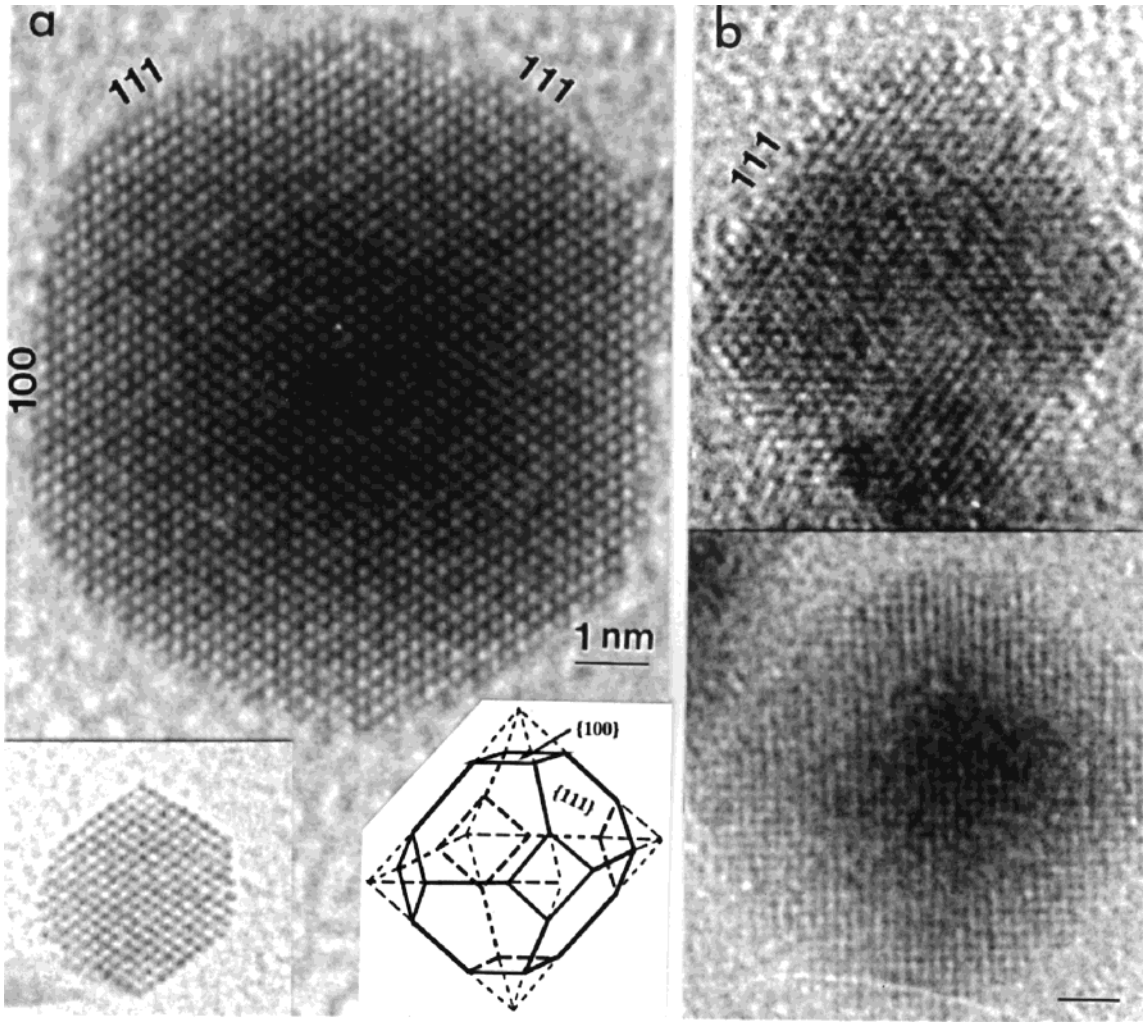

Figure 7. HRTEM images of Pt nanocrystals (a) with a truncated octahedral shape and oriented along [110] and (b) with a octahedral shape and oriented along [110] and [001]. The inset in (a) is a model of the particle shape (The Pt nanocrystals were supplied by Prof. M. A. El-Sayed's group).

$$I(x,y) \approx 1 - 2\sigma V_p(x,y) \otimes t_s(x,y,\Delta f) \qquad (8)$$

where $t_s(x,y,\Delta f) = \mathrm{Im}[t_{obj}(x,y,\Delta f)]$. The second term in eq 8 is the interference result of the central transmitted beam with the Bragg reflected beams. Any phase modulation introduced by the lens would result in contrast variation in the observed image. The weak scattering object approximation fails in most practical cases, but it is the easiest and clearest way to illustrate the

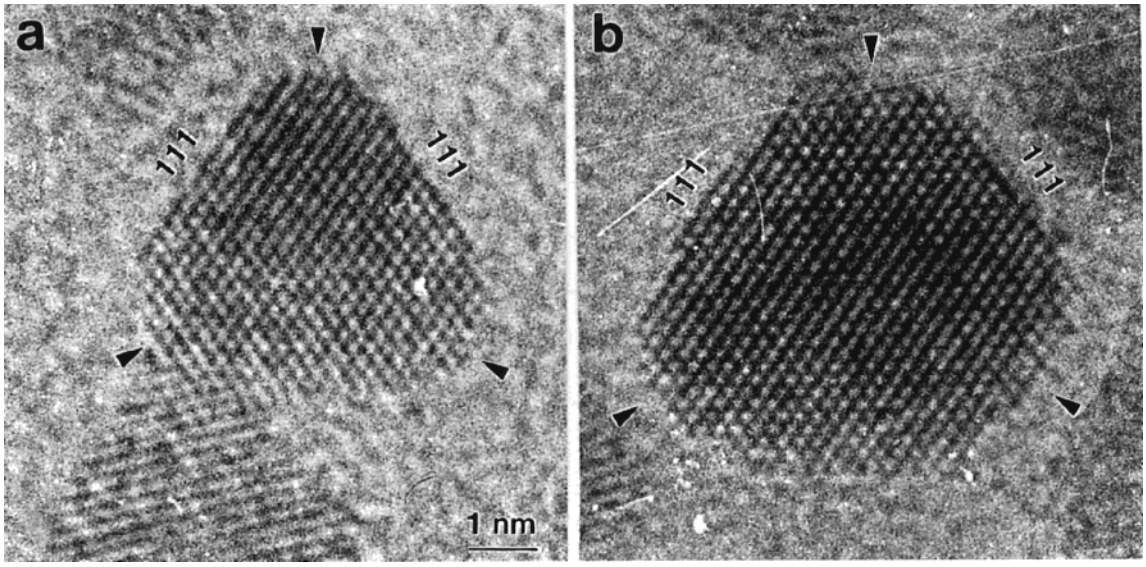

Figure 8. HRTEM images of truncated tetrahedral Pt nanocrystals oriented along [110]. The surface steps and ledges at the truncated corners are clearly resolved (The Pt nanocrystals were supplied by Prof. M. A. El-Sayed's group).

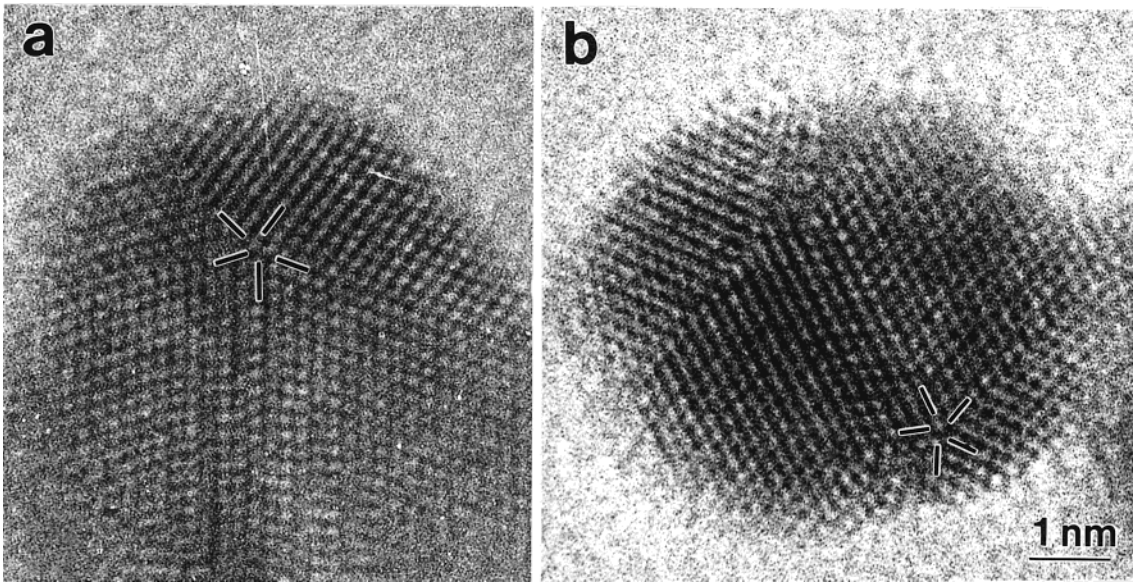

Figure 9. TEM images of decahedral Au nanocrystals when the incident electron beam is parallel or nearly parallel to the 5-fold symmetry axis (The Au nanocrystals were supplied by S. Link).

physics involved in HRTEM imaging. Equation 8 clearly shows that an TEM image is a two-dimensional projection of a three-dimensional object. The atom rows can be resolved clearly if their orientations are parallel to the incident beam. One must keep this in mind in interpretation of TEM images.

The optimum shape of the lens transfer function t_{obj} is a narrow Gaussian-like function with a small tail. The spherical aberration coefficient C_s of a TEM is fixed, the only variable is the objective lens defocus Δf. Under the Scherzer defocus,[16] $\Delta f = (^4/_3 C_s\lambda)^{1/2}$, $t_s(x, y, \Delta f)$ is approximated to be a negative Gaussian-like function with a small oscillation; thus, under the WPOA, the image is directly related to the two-dimensional thickness-projected potential of the crystal and the atoms show dark contrast. This is the basis of structure analysis using HRTEM. On the other hand, the form of the $t_s(x,y,\Delta f)$ function depends on the defocus of the objective lens; contrast reversal is possible simply by changing the defocus of the objective lens. Therefore, the occurrence of dark atoms or bright atoms in the image is determined largely by the defocus value.

For a general case, image simulation is required to quantify the information provided by HRTEM. The dynamic diffraction process is to solve the Schrödinger equation under given boundary conditions. There are several approaches for performing dynamic calculations.[17] For a finite crystal containing defects and surfaces, the multislice theory[18] is most adequate for numerical calculations. This theory has the unique advantage of fully accounting for the defects, surfaces, particle shapes, and interfaces in image calculation. Shown in Figure 3 are simulated images of a decahedral Au particle in different orientations under two defocus conditions.[19] At the Scherzer defocus (Figure 3a), the atoms are dark, while the contrast is reversed at defocus $\Delta f = 70$ nm (Figure 3b). The contrast reversal is introduced mainly due to the phases introduced by the defocus to the beams that contribute to the image. On the other hand, the particle shape is apparent only if the decahedron is oriented along its 5-fold symmetry axis. This may give some experimental difficulties of estimating the population of decahedra in a specimen.

2.4. The Bright-Field, Dark-Field, and High-Resolution Lattice Imaging. There are two basic modes of TEM operation,

namely, the bright-field mode, where the (000) transmitted beam contributes to the image, and the dark-field imaging mode in which the (000) beam is excluded. The size of the objective aperture in the bright-field mode directly determines the information to be emphasized in the final image. When the size is chosen so small so as to exclude all of the diffracted beams, one has the configuration normally used for low-resolution imaging of defects, called diffraction contrast. In this case, a crystalline specimen is oriented to give a particular diffracted beam, or a systematic row of reflections and the image is sensitive to the differences in specimen thickness, distortion of crystal lattices due to defects, strain, and bending. High-resolution imaging is usually performed in bright-field mode by including a few Bragg diffracted beams within the objective aperture. When a crystal is oriented along one of its low-index zone axes (e.g., [110] or [100]), strong Bragg reflected beams are present. The lattice images are the result of interference among the Bragg reflected beams and the central transmitted beam, forming the *phase contrast* image.

Parts a and b of Figure 4 compare the ray diagrams for forming the bright-field and dark-field images. The dark-field mode involves the tilt of the incident beam by a pair of deflection coils to bring the diffracted beam, to be selected for imaging, parallel to the optic axis for reducing the spherical aberration effect. Recording of high-resolution images is the same as in the case of bright-field imaging except with a larger size objective aperture (Figure 4c). The most important factors in HRTEM are the astigmatism of the objective lens and the adjustment of the lens defocus. The latter critically affects the image contrast.

3. Structures of Individual Nanocrystals

3.1. Shapes of Polyhedral Nanocrystals. Surface energies associated with different crystallographic planes are usually different, and a general sequence may hold, $\gamma_{\{111\}} < \gamma_{\{100\}} < \gamma_{\{110\}}$. For a spherical single-crystalline particle, its surface must contain high-index crystallography planes, which possibly result in a higher surface energy. Facets tend to form on the particle surface to increase the portion of the low-index planes. Therefore, for particles smaller than 10−20 nm, the surface is a polyhedron. Figure 5a shows a group of cubooctahedral shapes as a function of the ratio, R, of the growth rate in the ⟨100⟩ to that of the ⟨111⟩. The longest direction in a cube is the ⟨111⟩ diagonal, the longest direction in the octahedron is the ⟨100⟩ diagonal, and the longest direction in the cubooctahedron ($R = 0.87$) is the ⟨110⟩ direction. The particles with $0.87 < R < 1.73$ have the {100} and {111} facets, which are named the truncated octahedral (TO). The other group of particles has a fixed (111) base with exposed {111} and {100} facets (Figure 5b). An increase in the area ratio of {111} to {100} results in the evolution of particle shapes from a triangle-based pyramid to a tetrahedron.

If the particle is oriented along a low-index zone axis, the distribution of atoms on the surface can be imaged in profile, and the surface structure is directly seen with the full resolution power of a TEM.[20] This is a powerful technique for direct imaging the projected shapes of nanoparticles, particularly when the particle size is small. Figure 6a gives a profile HRTEM image of cubic Pt nanocrystals oriented along [001]. The Pt particles were prepared by reduction of K_2PtCl_4 by hydrogen gas in the presence of polymer.[14,21,22] The particle is bound by {100} facets, and there is no defect in the particle volume. The distances between the adjacent lattice fringes are the interplanar distance of Pt {200), which is 0.196 nm, and the bulk structure

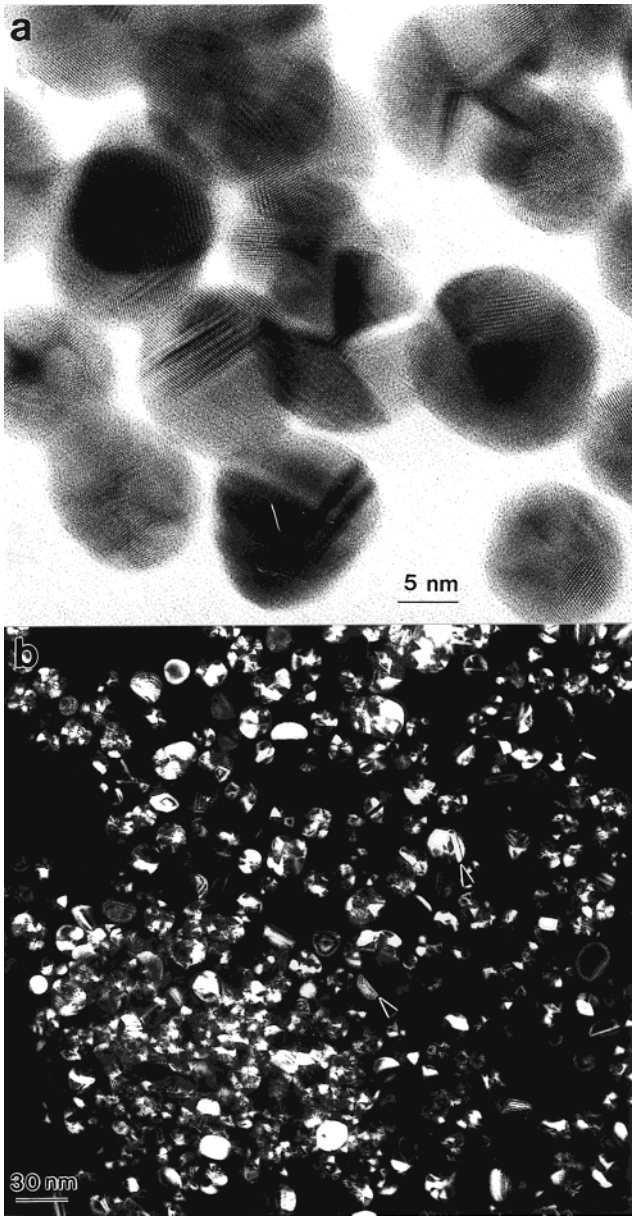

Figure 10. (a) A high-resolution TEM image showing the presence of twinning in Au nanoparticles. (b) A dark-field image recorded using a small section of the {111} and {200} reflection rings displaying the distribution of twinned particles in the specimen.

is face-centered cubic. The surface of the particle may have some steps and ledges particularly at the regions near the corners of the cube. To precisely image the defects and facets on the cubic particles, a particle oriented along [110] is given (Figure 6b). This is the optimum orientation for imaging cubic structured materials. In additional to the {111} and {100} facets, {110} facets are also observed, although they are considered as the surfaces with higher surface energy. The {110} facets are rather rough, and the {111} facets are present. These higher energy structural features are present because the particles were prepared at room temperature.

An octahedron has eight {111} facets; four {111} facets are edge-on if viewed along [110]. If the particle is a truncated octahedron, six {100} facets are created by cutting the corners of the octahedron, two of which are edge-on while viewing along [110]. Parts a and b of Figure 7 show the HRTEM images of [110] oriented truncated octahedron and octahedral Pt particles, respectively. A variation in the area ratio of {100} to {111} results in a slight difference in particle shapes.

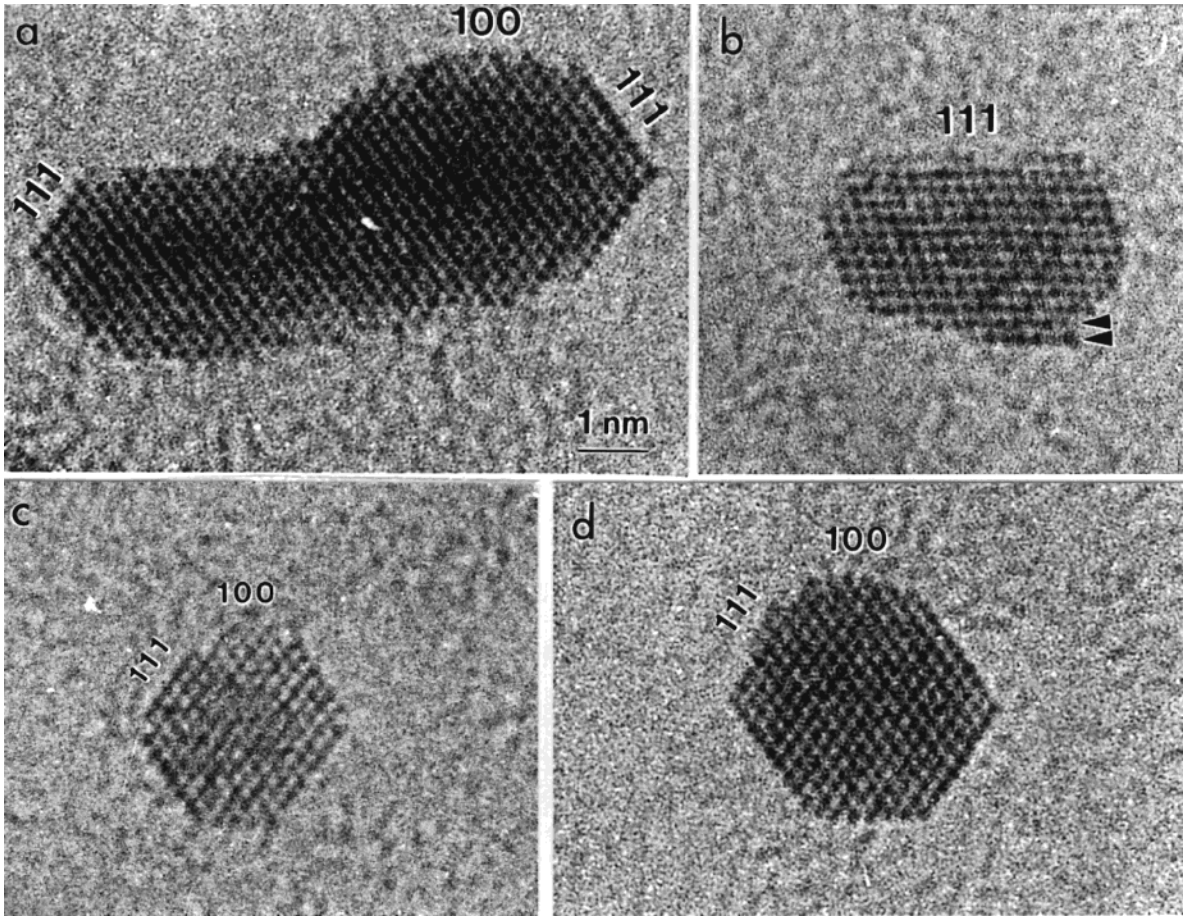

Figure 11. HRTEM images of Pt nanocrystals oriented along [110], showing the reconstructed {100} surfaces and surface relaxation (indicated by arrowheads, where the interlayer distance is slightly larger than that between the layers inside the volume).

A tetrahedral particle is defined by four {111} faces, and it usually gives a triangular shape in HRTEM.[23] Figure 8 gives two HRTEM images of truncated tetrahedral particles oriented along [110]. Two {111} facets and one {001} facet (at the top of the image as a result of truncation) are images edge-on. There are some atom-high surface steps on the {111} surfaces and the corners. These atomic rough structures are likely important for enhancing the catalysis activities of the nanocrystals.

3.2. Twinned and Multiply Twinned Nanocrystals. Twinning is one of the most popular planar defects in nanocrystals, and it is frequently observed for face-centered cubic (fcc) structured metallic nanocrystals. Twining is the result of two subgrains sharing a common crystallographic plane; thus, the structure of one subgrain is the mirror reflection of the other by the twin plane. The fcc structured metallic nanocrystals usually have {111} twins. The two most typical examples of multiply twinned particles (MTP) are decahedron and icosahedron.[24,25] Starting from an fcc structured tetrahedron, a decahedron is assembled from five tetrahedrals sharing an edge (Figure 5c). If the observation direction is along the 5-fold axis and in an ideal situation, each tetrahedron shares an angle of 70.5°, five of them can only occupy a total of 352.6°, leaving a 7.4° gap. Therefore, strain must be induced in the particle to fill the gap.[26] An icosahedron is assembled using 20 tetrahedra via sharing an apex (Figure 5d). The icosahedral and decahedral particles are the most extensively studied twinned nanocrystals.[27,28] The easiest orientation for identifying the MTPs is along the 5-fold symmetry axis.

Figure 9 shows two MTP Au particles, where the 5-fold axis is clearly seen. The particle given in Figure 9a is a single decahedral particle, while the one given in Figure 9b is a particle constituted of two decahedra. Twinning is the mechanism for forming these particles. The multiple twinning is the favorable structural configuration when the particles are small,[29] possibly because of the smaller surface and volume energies.

The presence of stacking faults and twins in the nanocrystals may strongly affect their optical properties. The fraction of twinned particles can be reasonably evaluated using dark-field imaging, which is formed by selecting a small segment of the {111} and {200} reflected rings. The particles with orientations that can produce strong Bragg reflections falling into the angular selection range of the objective aperture in TEM show bright contrast, provided the particles are single crystalline. For the twinned particles, however, part of the particles may show bright contrast and the other parts are darker, providing an easy technique for identifying the presence of twins and their distribution among the particles. Figure 10 gives such an example. The particles having twin structure are partially diffracting the electrons into the angular range selected by the objective aperture and the remaining parts show darker contrast. The high magnification image clearly shows the twinned structure and the strain induced by the twin structure (Figure 10a), and the low magnification dark-field image unambiguously illustrates the distribution of twins (Figure 10b).

3.3. Surface Defects. Simply speaking, surface atoms have less bonds in comparison to the atoms in the bulk because of the loss in nearest neighbors. The surface atoms tend to find new equilibrium positions to balance the forces, resulting in surface reconstruction and defects. Figure 11 gives a group of images recorded from Pt nanocrystals. The {111} faces in parts a, c, and d of Figure 11 are relatively flat, while the {100} types of faces show a large deviation from the perfect lattice structure,

suggesting the occurrence of a nonordered surface reconstruction. Surface relaxation is clearly seen in Figure 11b in the layers indicated by arrowheads. Nanocrystals have larger surface energy and the surface defects are believed to be abundant. The surface atoms are likely to have dangling bonds, resulting in higher surface reactivity. The {110} surface is rarely seen possibly because of higher surface energy. The Au {110} surface in nanoparticles has been found to be reconstructed so that the surface is composed of corners bound by {100} mini-facets, e.g., the Au atoms are missing every other row parallel to the [110] direction.[30]

3.4 Imaging of Ultrasmall Particles. High-resolution TEM image of crystalline specimens is the result of electron wave interference among diffracted Bragg peaks. If the number of atoms in a particle is so small that no significant diffraction will be generated, high-resolution TEM is unlikely to reveal the intrinsic structure of the cluster. Therefore, the question is how small can a particle be before HRTEM becomes ineffective in identifying its shape? To answer this question, we have tried to image the Pt atom clusters that were nucleated at the beginning of the growth. A lower magnification image of the particles dispersed on a carbon substrate shows the coexistence of large size as well as small size particles (Figure 12a), where the smaller particles are dominated by tetrahedra and truncated octahedra, while the large particles are dominated by cubic. This shape transformation from tetrahedral-to-octahedral-to-cubic is the result of the kinetically controlled growth.[31] Small size clusters of truncated octahedra can be imaged (Figure 12b). The number of atoms presented in these particles may be 225 and 79 provided the particle shapes are perfect.

3.5. Faceted Shape of Rodlike Nanocrystals. Nanocrystals can have a wide range of shapes. The gold nanorods recently synthesized by a reverse miscell technique are rather unique.[32] The rod is bounded by facets and it is a thermodynamically unstable crystal growth. Almost all of the Au nanorods are single crystalline and contain no twins or dislocations.[6] When the liquid droplet containing the suspended Au nanorods was dispersed onto a flat carbon substrate, the nanorods were preferentially aligned and oriented along [110] perpendicular to the substrate (Figure 13a). The single Au nanorods also prefer to orient along [110] (Figure 13b). This is possible only if the nanorods have {110} facets. A dark-field TEM image recorded using a {111} reflected beam when the rod is oriented nearly parallel to the [110] direction gives the thickness fringes (Figure 13c) owing to thickness variation across the specimen. The intervals between the fringes would have an equal distance if the nanorods were bound only by four {100} facets. The finite width of the band at the center and its uniformity in intensity indicate that the thickness at the center region is nearly constant with a width of ~5 nm, strongly supporting the presence of {110} facets. The axial growth direction is [001], and its cross section is given in Figure 13d.

3.6. Electron Beam Effect. In HRTEM, nanocrystals are illuminated by an intensive electron beam; thus, radiation damage is inevitable. Radiation damage can be due to ionization of the atoms, breaking bonds, local heating, and knock-on displacements. Which of these takes the dominant role depends on the material and the accelerating voltage, the electron dose, and the dose rate of the microscope. For particles smaller than 5 nm, the electron beam can result in structural transformation and/or rotation of nanocrystals,[33,34] and these effects are enhanced as the particle size decreases. As we know that radiation damage is inevitable in TEM, one must learn how to identify the true structure of the nanocrystal from the information provided by TEM. For particles larger than 5 nm, the beam effect is quite small.

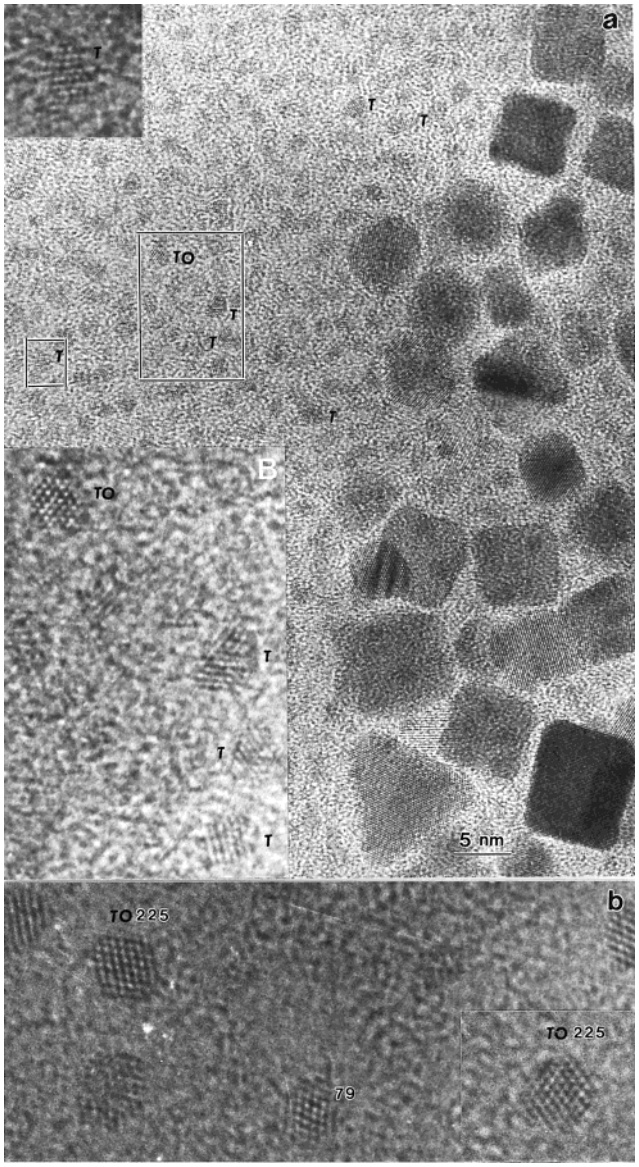

Figure 12. HRTEM image of Pt nanocrystals whose shapes were dominated by tetrahedra when they are small, but a transformation to cubic shape occurred as they grow larger. (b) The possible "smallest" nanocrystals whose shape still can be identified by HRTEM. The numbers represents the possible of numbers of atoms in the particles if they are perfect truncated octahedra without point defects.

4. Structures of Self-Assembled Nanocrystal Arrays

Size- and even shape-controlled nanoparticles behave like molecules that can be taken as building blocks for constructing two- and three-dimensional cluster self-assembled superlattice structures.[35−39] Nanocrystal arrays are characterized by unprecedented size uniformity and translation and even orientation order. The nanocrystals are passivated by a monolayer of long-chain organic molecules, such as SR, where R = n-C_nH_{2n+1}, n = 4, 6, 8, 12 ..., called thiolates, that serve not only as the protection for the particles to avoid direct contact between the particles with a consequence of coalescing but also the interparticle bonding. By changing the length of the molecular chains, quantum transitions and insulator to conductor transition could be introduced, resulting in tunable electronic, optical, and transport properties.[40]

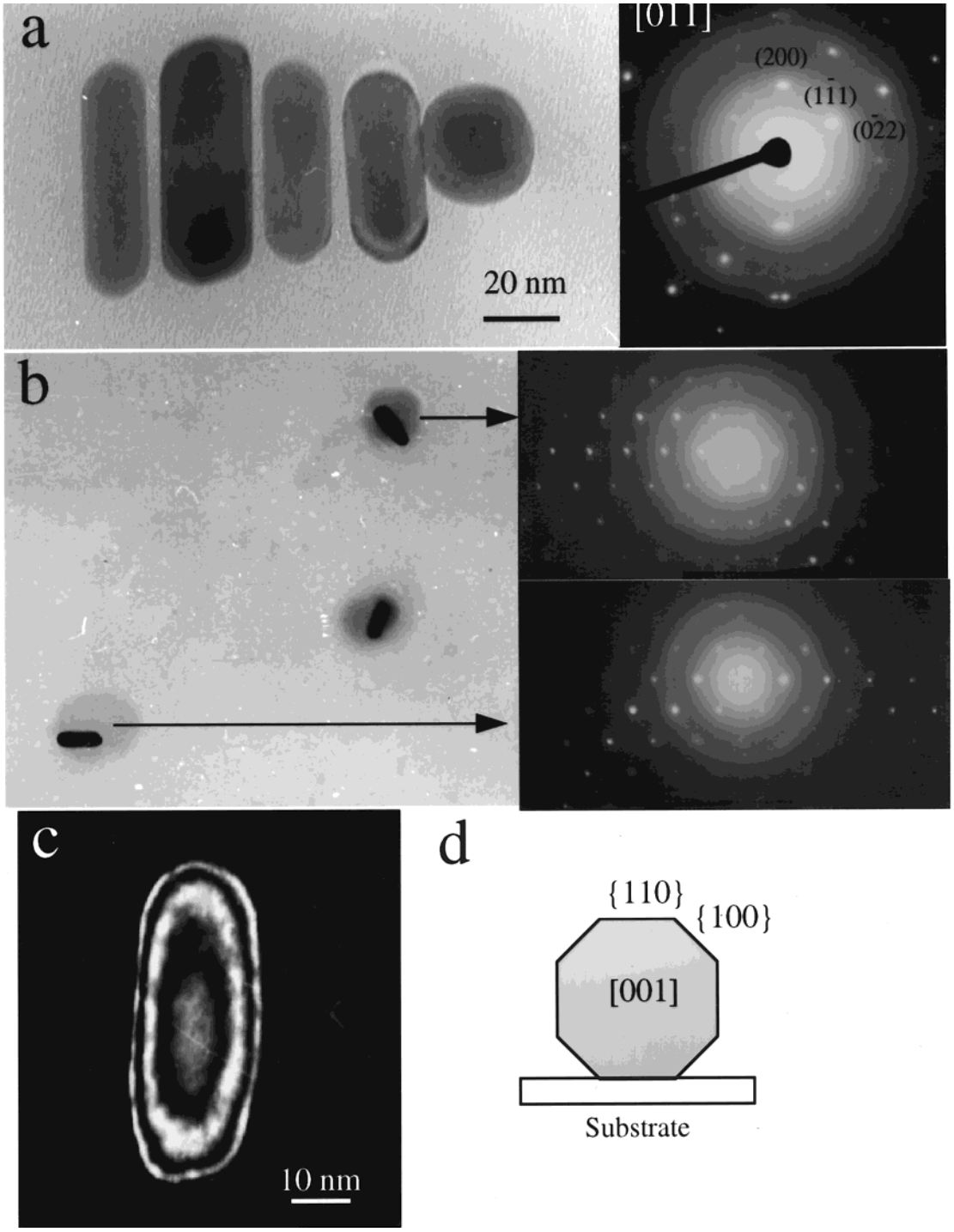

Figure 13. (a) Bright-field TEM image of Au nanorods and the corresponding electron diffraction pattern recorded from the first three rods aligned on the left, proving the unified [110] orientation of the rods. (b) Bright-field TEM image of individually dispersed Au nanorods, showing the [110] orientation perpendicular to the substrate. (c) Dark-field TEM image of an Au rod oriented nearly parallel to [110]. These images unambiguously suggest the formation of {110} facets on the nanorods. (d) The cross section of an Au rod on the substrate.

4.1. Particle Shape in Self-Assembly. If the nanocrystals can be taken as the building blocks, their 3-D assembly is unavoidably affected by the particle shape.[41,36] TEM is unique in determination of the relationship between particle orientations and the assembling crystallography of the ordered array. Figure 14a is an TEM image recorded from an Ag nanocrystal superlattice (NCS) deposited on a carbon substrate, from which the orientation of the particles and the arrays can be identified. The Ag nanocrystals have a truncated octahedral shape (Figure 14b), and they are oriented along the [110] of the Ag atomic lattice in the image, along which four {111} and two {100} facets are imaged edge-on. The unit cell of the NCS is also oriented along $[110]_s$ of fcc, where the subscript refers to the supercrystal. Therefore, the orientational relationship between the Ag particles and the nanocrystal lattice is [110] || $[110]_s$ and [001] || $[1\bar{1}0]_s$. This registered orientational order can be used to determined the orientations of the nanocrystals in the unit cell of the superlattice, as shown in Figure 14c. The nanocrystals are packed into a face-centered cubic lattice, and the nanocrystals are arranged following a principle of face-to-face [10]. The image recorded from the same area at a slightly large defocus condition gives the channels (the white dots in

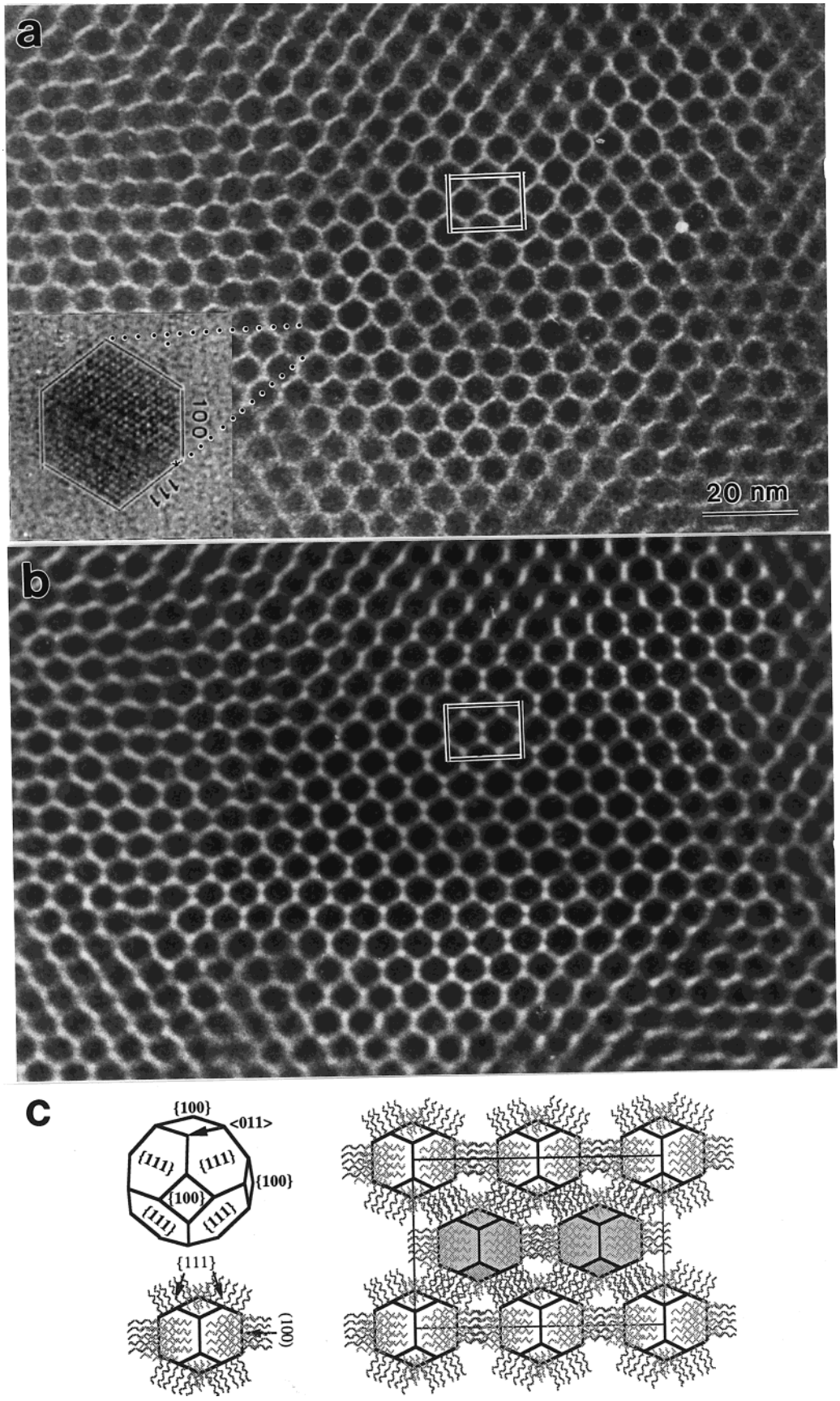

Figure 14. (a) TEM image of a face-centered cubic packed Ag nanocrystals whose shape is dominated by truncated octahedral (TO) (see the inset HRTEM image of a single Ag nanocrystal). The image displays the orientational relationship between the nanocrystals and the assembled superlattice. (b) A TEM image recorded from the same specimen area under slightly defocused condition. The image in (a) is recorded at near focus condition, and it is sensitive to the particle shape, and the image in (b) is most sensitive to the phases caused by a variation in the projected mass thickness. (c) A structural model of the TO particle and the $[110]_s$ projection of the unit cell as indicated in (a), where the gray pasted particles are located at different *z* heights. The channels enclosed by the bundled thiolates are presented.

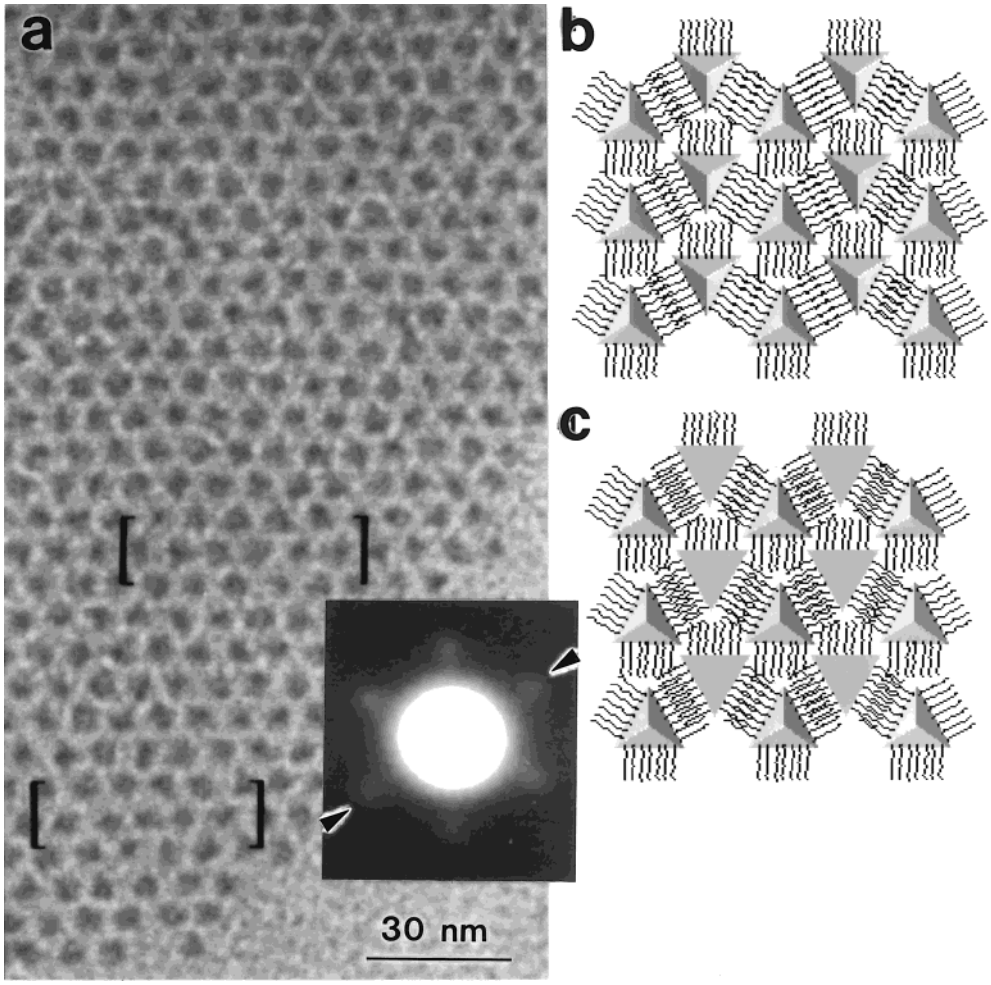

Figure 15. (a) TEM image of a monolayer self-assembly of tetrahedral Ag nanocrystals. (b and c) Two possible assemblies of tetrahedra with short-range orientational order. A small-angle electron diffraction pattern from the monolayer assembly, reflecting the mirror symmetry (not 3-fold) (The Ag nanocrystals were supplied by R. L. Whetten and S. A. Harfenist).

Figure 14b) enclosed by the bundling distributed thiolates molecules on the surface of the nanocrystals. This model has been proved by the energy-filtered chemical imaging technique in TEM.[42]

The self-assembly of nanocrystals is strongly affected by the shape of the nanocrystals. The tetrahedral shaped nanocrystals have sharp corners and their assembly may have long-range translational symmetry but the orientational order is limited only to a short range.[43] Figure 15a gives the monolayer self-assembly of tetrahedral Ag nanocrystals. Two fundamental principles are usually observed in particle self-assembling. The most dense packing is the favorable configuration from the energy point of view. The passivation molecules are likely to form interdigitative bonds that link the nanocrystals. Two possible monolayer assembly models satisfying the two requirements are given in parts b and c of Figure 15. The only difference between the two models is that half of the particles face down, while the projected structures of the two are identical. These models do not support the 3-fold symmetry of the packing due to the shape of the particles, in agreement with the mirror symmetry presented by the electron diffraction pattern (the inset in Figure 15a). The regions indicated by parenthesis in Figure 15a agree well with the models.

4.2 Dark-Field Imaging in Identification of Particle Shape. Particle shapes can be identified by high-resolution TEM images, but in some cases the dark-field imaging is indispensable for confirming the result. Figure 16 shows such an example of CoO nanocrystals.[44] The bright-field TEM images (parts a and c of Figure 16) illustrate that the particles have triangular-like projected shapes. The projected triangles may correspond to either tetrahedral or platelet-like structure. If the latter were the case, the dark-field image recorded using the diffracted electrons would show a uniform contrast across the particle because there is no variation in the projected thickness across the particle. In contrast, the dark-field image (Figure 16b) shows bright spots at the center of some particles, indicating the tetrahedral shape because the dark-field image is sensitive to the projected density of the atoms under the first-order scattering approximation. On the other hand, the bright-field image given in Figure 16c cannot uniquely define the particle shape.

Dark-field imaging can also be useful for identifying the number of stacking layers in particle self-assembling.[45] Figure 17 is such an example, which was recorded by positioning a small size objective aperture on the optic axis while the incident beam is scanned conically to average over the particle orientations. This type of image is called conical scan dark-field imaging and it is most sensitive to the local projected mass thickness, and the diffraction effect is minimized. The monolayer assembly preserves very well the translational symmetry. The second layer introduces a minor short-range disorder, while the third layer is largely disordered. The reason for the increased disordered structure is likely due to the introduction of larger size particles, resulting in the creation of "interstitial" and vacancy point defects in the arrays. The contrast of this type of

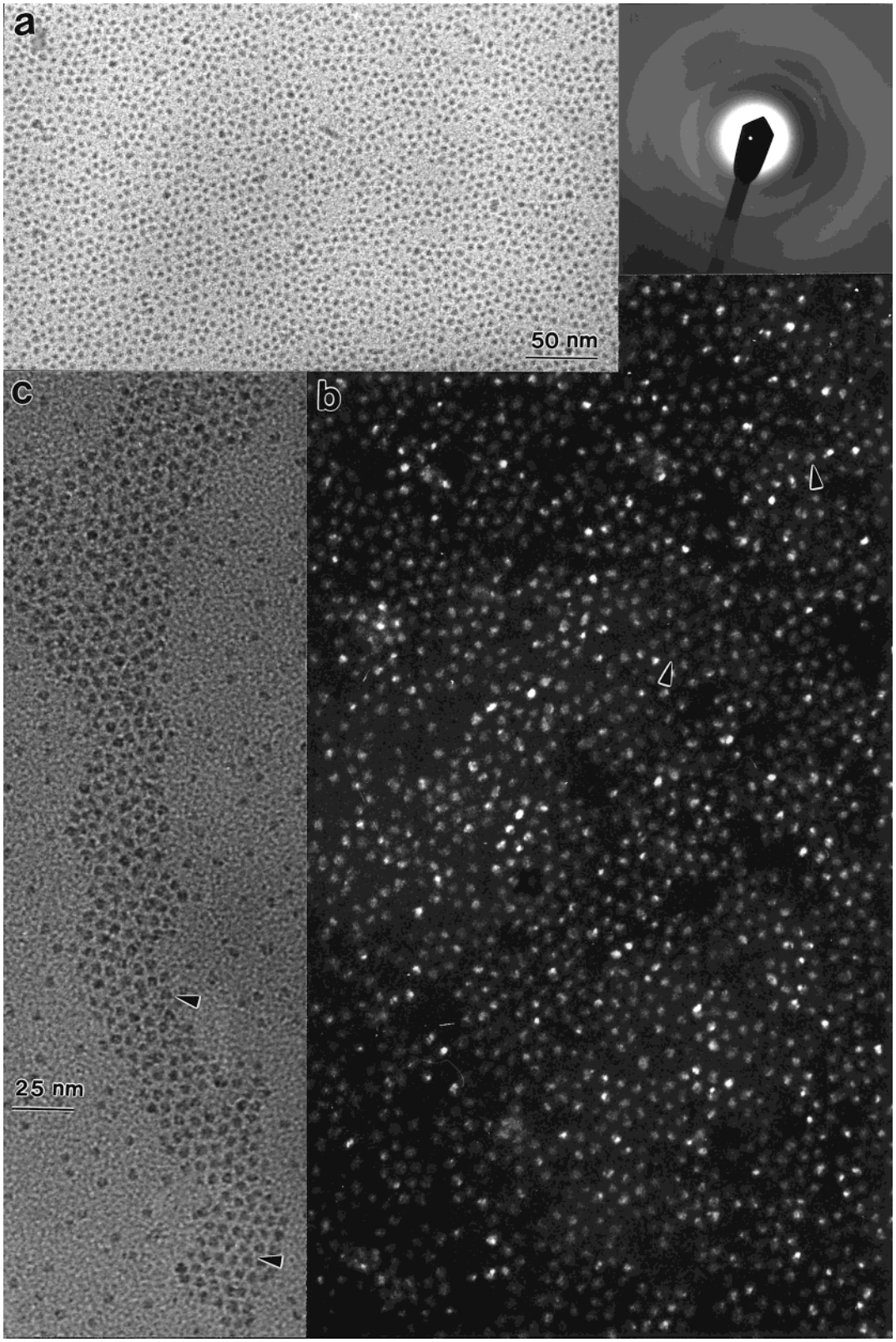

Figure 16. (a, c) Bright-field and (b) dark-field TEM images of monolayer self-assembly of tetrahedral CoO nanocrystals of ~4 nm in size, displaying short-range translational ordering but no orientational order. An electron diffraction pattern from the nanocrystals is shown in the inset, exhibiting broadened rings.

image is proportional to the specimen thickness for relatively thin specimens, allowing for a direct identification of the number of stacking layers from the image.

We have shown in Figure 16c that tetrahedral nanocrystals gives triangular projections in the TEM image. However, a triangular pattern observed in the bright-field image in a self-assembled array may not prove the tetrahedral shape of the nanocrystals. Figure 18a shows a bright-field TEM image recorded from the ordered array of Ag nanocrystals. The image clearly shows some triangular-shape contrast, in which the triangles are as if representing the nanocrystals (in dark contrast). A conical scan dark-field image recorded from the same region

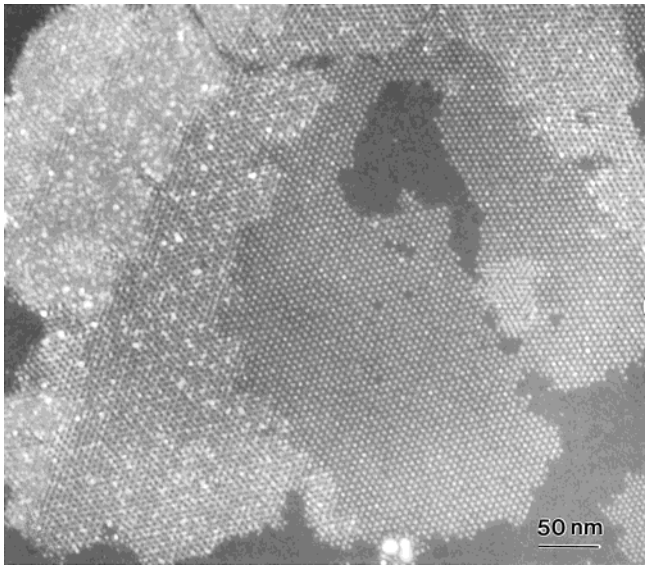

Figure 17. Dark-field TEM image recorded by scanning the incident beam conically, showing the monolayer, double-layer, and triple-layer self-assembly of Ag nanocrystals (The Ag nanocrystals were supplied by S. A. Harfenist).

of the specimen, in which the particles show bright contrast, proves that the particles have a nearly spherical shape (Figure 18b) because the bright contrast area in this image usually represents the objects with a larger mass thickness; the triangles are in darker contrast corresponding to the cavities among the particles. Thus, the particles cannot be tetrahedra. To explain this imaging phenomenon, a hexagonal close packed A−B−A−A−B stacking sequence is created for an odd number of layers (Figure 18c). The stacked layers create a channel of close to a triangular shape if the projected mass is considered, which corresponds to the darker contrast triangle observed in the dark-field image. Image simulations have confirmed this type of interpretation.[46] Alternatively, an examination of the dispersed particles can also provide additional proof about the particle shape.

5. In Situ Temperature-Induced Structural Evolution of Nanocrystals

In situ study of the temperature-induced phase transformation and structural and chemical evolution of nanocrystals is important for understanding the structure and structural stability of nanomaterials. TEM is an ideal approach for conducting these types of experiments, in which a specimen can be cooled to the liquid nitrogen or liquid helium temperatures or heated to 1000 °C. The in situ process can be recorded at TV rate for exhibiting the time and temperature-dependent phenomena.

The large percentage of surface atoms in nanocrystals is the origin of their unique properties. The melting of Pt particles[42] and the surface sublimation of Au nanorods[6] are taken as examples here to illustrate the unusual thermodynamic properties of nanocrystals. Platinum nanoparticles with a high percentage of cubic-, tetrahedral-, and octahedral-like shapes, respectively, have been synthesized by changing the ratio of the concentration of polymer capping material (polyacrylate) to that of Pt^{2+} being reduced by H_2 from K_2PtCl_4 at room temperature.[14,47] The polymer acts not only as the passivative protection layer of the nanocrystals but also as the key factor in controlling their shapes. To determine the shape-dependent catalytic behavior of Pt nanocrystals, the passivation layer on the nanocrystal must be removed. Several questions remain to be considered: (1) how high does the annealing temperature need to be to remove the capping polymer while the particle shape is still preserved?; (2) to what temperature is the particle shape still stable?; (3) how high is the melting point of the Pt particles? In situ TEM observation of the particle shape transformation and melting can provide answers to these questions.

Figure 19 shows a series of TEM images recorded from the same region when the specimen temperature was increased from 25 to 610 °C. These images were selected from a group of images to present the most significant changes in the particle shapes. For easy notation, particles are labeled as groups to trace their shape transformation behavior. Most of the particle shapes showed no significant change when the specimen temperature was below 350 °C (parts a−c of Figure 19). Truncated cubic and tetrahedral particles were formed when the temperature arrived at 410 °C (Figure 19d). The corners and edges of the particles were disappearing because the local atoms have higher energy. The tetrahedral particles could still be identified even when the temperature reached 500 °C (Figure 19e), while the cubic particles became spherical when the temperature was above 500 °C. This indicates that the tetrahedral particles are more stable than cubic ones possibly because the {111} surfaces have lower surface energy than the {100}. A feature observed in Figure 19 is that the tetrahedral shape of a particle indicated by an arrowhead was preserved when the specimen temperature was as high as 610 °C. This is possibly due to the contact of the apexes of the particle with the adjacent particles so that the interparticle diffusion can still sustain the shape of the apexes. Our results indicate that the surface capping polymer is removed by annealing the specimen to a temperature of 180−250 °C, while the particle shape shows no change up to ∼350 °C. In the temperature range 350−450 °C, a small truncation occurs in the particle shape but no major shape transformation. The particle shape experiences a dramatic transformation into a spherical-like shape when the temperature is higher than ∼500 °C (the melting point of bulk Pt is 1773 °C).

The thermodynamic properties of nanocrystals depend strongly on not only the crystal size but also their shapes. The thermodynamic properties of Au nanorods is an example.[6] No structural change is observed at temperatures below 215 °C. However, some tiny Au clusters appeared on the substrate as the temperature arrived at 230 °C (Figure 20c). The clusters grew rapidly as temperature increased to 350 °C, above which the clusters shrank in size (parts f−h of Figure 20). The Au clusters are believed to be formed by the atoms sublimated from the nanorod surfaces due to the presence of the high energy {110} faces.[6] Since the supply of the atoms to the cluster is proportional to its contact length with the substrate (proportional to the particle radius r) and the sublimation is proportional to the surface area of the cluster (r^2), the clusters grew faster when they are small because of the dominant r term. The shrinkage of the clusters at higher temperatures is due to the increased sublimation rate. An interesting phenomenon observed in Figure 20 is that the nanorod indicated by an arrowhead shrank as temperature went up, but it regrew at sufficiently high temperature. This reversed atom diffusion is likely to be associated with its interaction with the neighboring rods.

To reveal the unique surface processes associated with Au nanorods, the rods were photoisomerized to form gold nanospheres by the influences of femtosecond laser pulses.[48,49] Both the nanospheres and nanorods have the same average volume and almost equally exposed surface areas (with consideration of the contact of the particle with the substrate); thus, the size effect of the two geometrical shapes should not make a

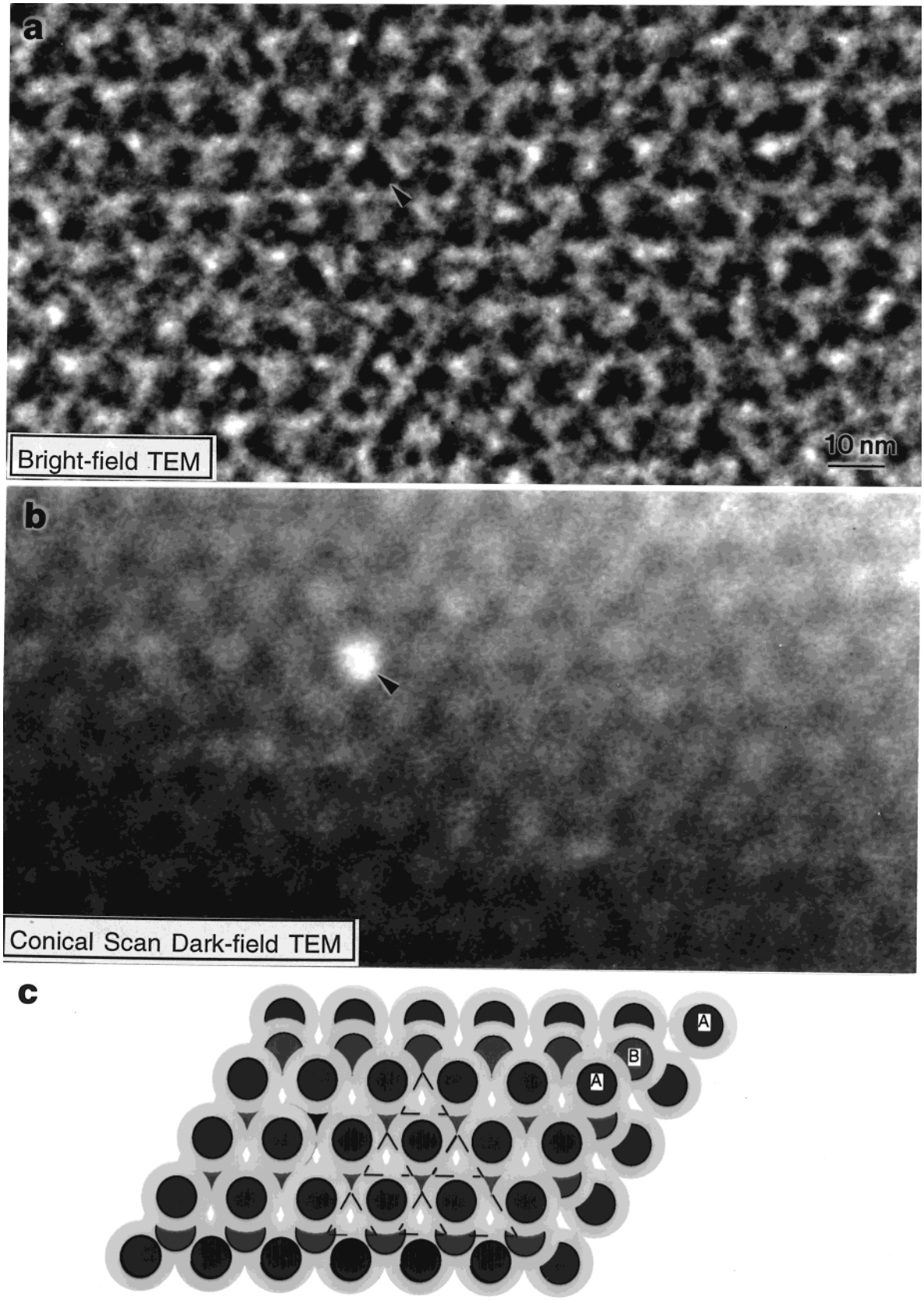

Figure 18. (a) Bright-field and (b) conical-scan dark-field TEM images recorded from same region of a multilayer self-assembly of Ag nanocrystals. (c) A model for interpretation of the image contrast.

significant difference. After being heated to as high as 650 °C, no clusters were formed near the gold nanospheres. This clearly shows that the newly formed Au particles are unique characteristics of Au nanorods. Using HRTEM, it has found that the nanorods have the unstable {110} facets (see Figure 13), in addition to the {100} and {111} facets present in the spheres. The presence of a significant percentage of gold atoms on the {110} surface suggests that the nanorod is relatively thermodynamically unstable. The {111} and {100} faceted Au spheres have lower surface energy. Thus, their atoms may not sublime

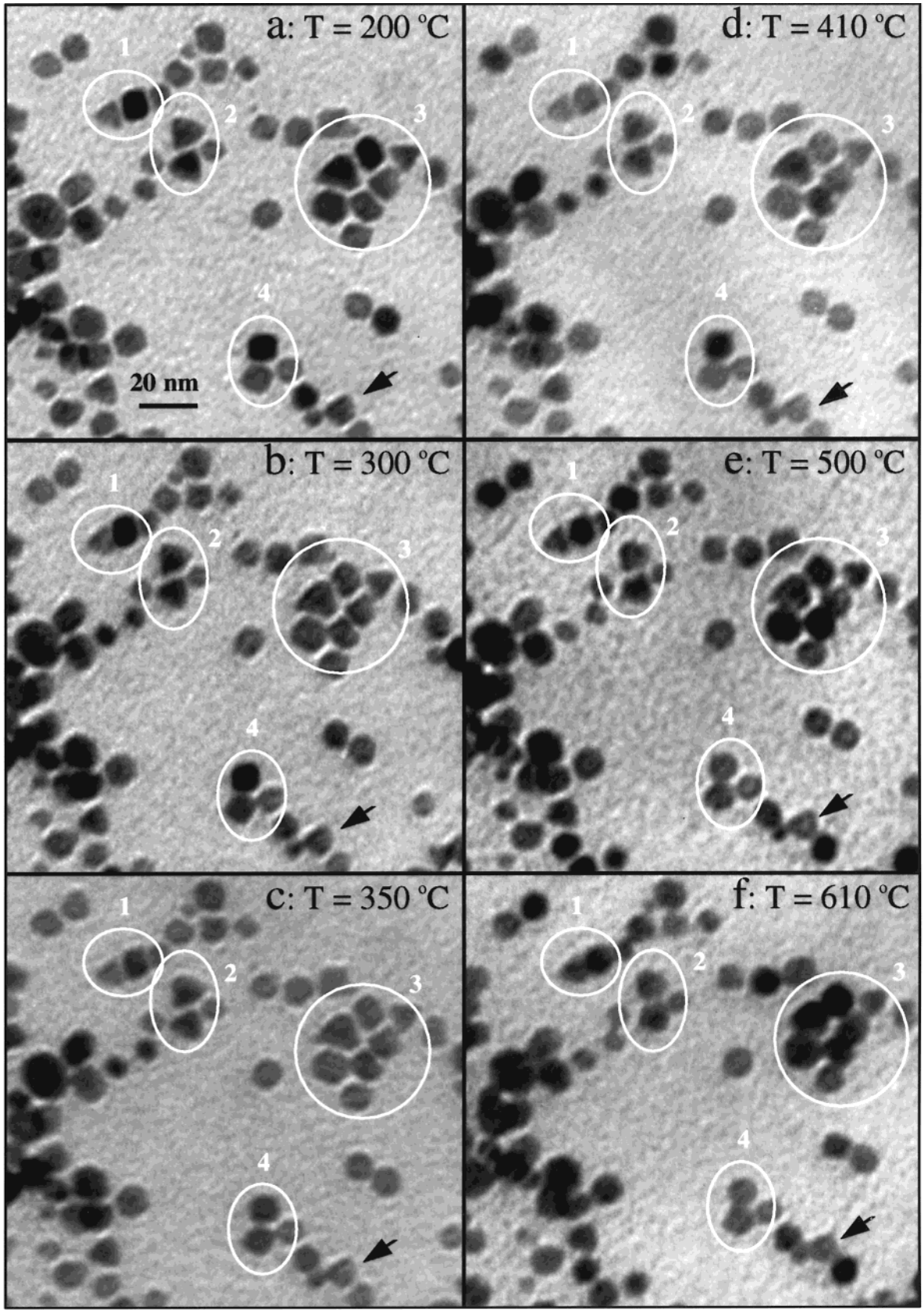

Figure 19. A series of TEM images recorded in situ from Pt nanocrystals dispersed on a carbon substrate and being heated to different temperatures, exhibiting the shape transformation as well as surface melting phenomenon of the particles at temperatures much lower than the melting point of the bulk (The Pt nanocrystals were supplied by J. Petroski and M. A. El-Sayed).

at relatively lower temperatures. Therefore, the sublimation of Au atoms from the nanorods at lower temperatures is due to the shape of the nanorods, which has the unstable {110} surfaces.

In situ TEM is also a powerful approach to examine the structural evolution of nanocrystal self-assembled arrays. The ordered assembly of Ag nanocrystals of ~5 nm in core size preserves the order to a temperature as high as 500 °C, much

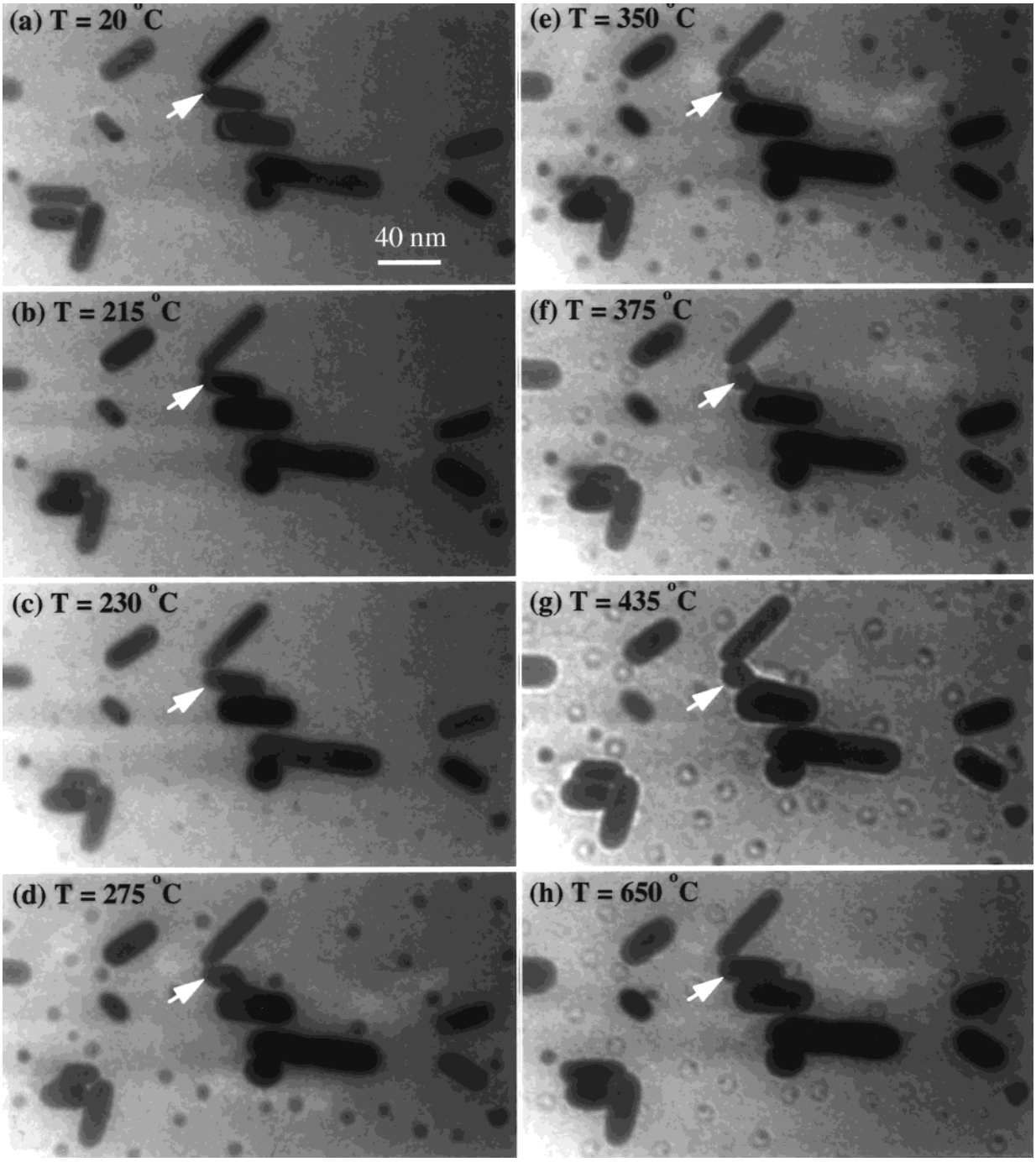

Figure 20. TEM images of the Au nanorods recorded in situ at different temperatures, illustrating the nucleation and growth of Au clusters on the substrate. The Au clusters are the condensation of the sublimated Au atoms from the nanorods (The Au nanocrystals were supplied by M. Mohamedi and M. A. El-Sayed).

higher than the expected temperature.[50] This is likely due to the strengthened binding force owing to the formation of the interdigitative molecular bonds of the adsorbed molecules on the nanocrystal surfaces. Monolayer self-assembly has been found to exhibit the highest thermal stability,[51] possibly because of the strong effect from the carbon substrate.

6. Measuring the Properties of Individual Nanostructure by In Situ TEM

There are four key steps in the development of nanoscience and nanotechnology: materials preparation, property characterization, device fabrication, and system integration. Because of the high size and structure selectivity of the nanomaterials, their physical properties could be quite diverse. An essential task in nanoscience is the property associated characterization of an individual nanostructure with well-defined atomic structure. But as limited by the size of the nanostructures, new methods and methodologies must be developed to manipulate and quantify the properties of individual nanostructures. It is important to directly view the nanostructure while a testing or measurement is being carried out.

We have recently applied TEM as a means of nanomeasurement in characterizing the mechanical strength of a single carbon nanotube.[52] Carbon nanotube has a nanofiber-like structure consisting of concentric cylindrical graphitic sheets, with diameters of 5−50 nm and lengths of 1−20 μm. A TEM

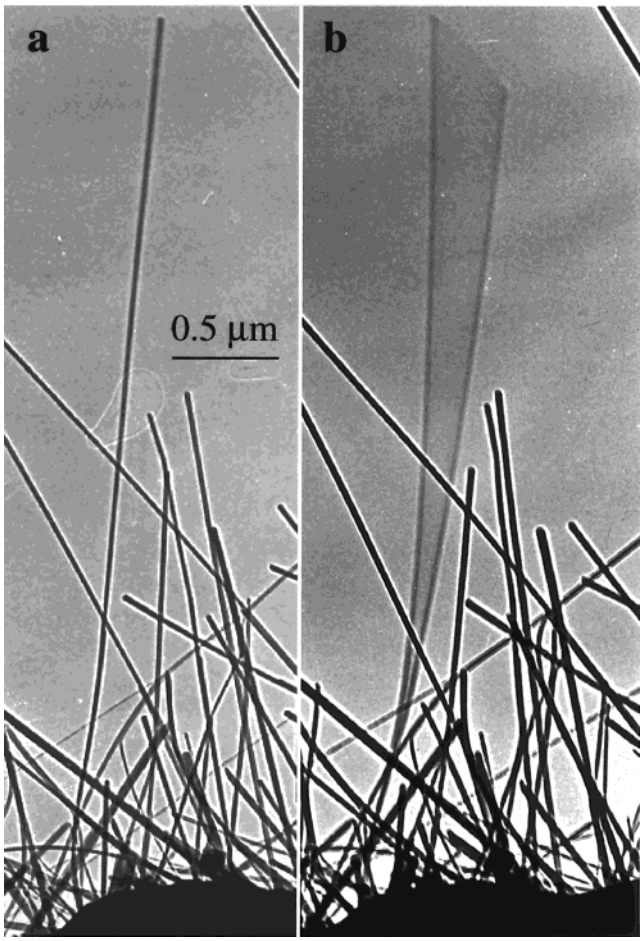

Figure 21. Alternating field-induced mechanical resonance. A selected carbon nanotube at (a) stationary and (b) the first harmonic resonance (ν = 1.21 MHz) (in collaboration with P. Poncharal and W. A. de Heer).

specimen holder was specially built for applying a voltage across the nanotube and its counter electrode. Each single nanotube can be clearly observed in the TEM. Thus, the measurements can be done on a specific nanotube whose microstructure is determined by transmission electron imaging and diffraction. If an alternating voltage is applied on the nanotube with an ability to tune the frequency of the applied voltage, resonance can be induced when the frequency of the applied voltage equals the natural frequency of the nanotube (Figure 21). Thus, the bending modulus of nanotubes can be calculated from the resonance frequency. This is likely to be the most precise method for characterizing the mechanical properties of a single fiberlike structure, providing a simple approach toward nanomechanics.

Similar to a cantilevel pendulum and using the carbon nanotube with a calibrated bending modulus, the mass of a tiny particle attached to the end of the nanotube can be determined from the vibration frequency. For the case shown in Figure 22, the mass of the particle is determined to be 22 ± 6 fg (1 fg = 10^{-15} g). This is the newly discovered "nanobalance", the most sensitive and smallest balance in the world.[52] We anticipate that this nanobalance will have applications in measuring the mass of large biomolecules and biomedical particles, such as virus, possibly leading to a nanomass spectrometer. Using the in situ TEM specimen holder we built, the ballistic quantum conductance in defect-free carbon nanotubes[53] has been repeated, and the characteristics of electron field emission from individual carbon nanotube is under investigation.

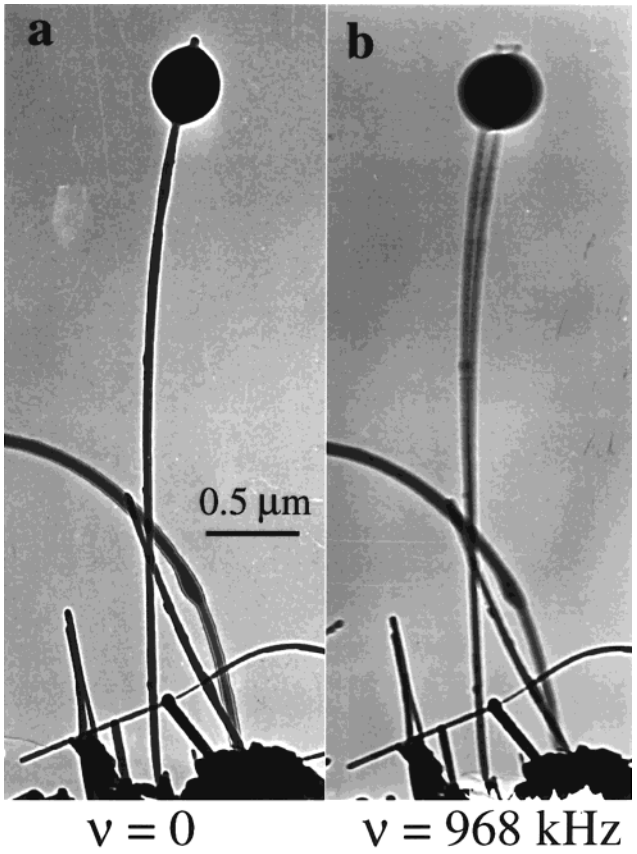

Figure 22. A small particle attached at the end of a carbon nanotube at (a) stationary and (b) the first harmonic resonance (ν = 0.968 MHz). The mass of the particle was determined to be 22 fg (in collaboration with P. Poncharal and W. A. de Heer).

7. Chemical, Electronic, and Bonding Structures of Nanocrystals

7.1. Chemical Microanalysis by EDS and EELS. HRTEM is a powerful technique for identifying the crystal structure of nanophase materials, but it may not be sensitive enough to detect a small change in atomic number. To precisely determine the content of a particular element in a specimen, energy dispersed X-ray spectroscopy and electron energy loss spectroscopy can be very useful. Under the impact of an incident electron, the electrons bounded to the atoms may be excited either to a free electron state or to an unoccupied energy level with a higher energy. The quantum transitions associated with these excitations will emit photons (e.g., X-rays) and Auger electrons. These inelastic scattering signals are the fingerprints of the elements that can provide quantitative chemical and electronic structural information. Two analytical techniques are most commonly used in chemical microanalysis in TEM, EDS,[54] and EELS.[12] The size of the incident electron probe can be as small as 2−3 nm, giving the feasibility of acquiring EDS and EELS spectra from individual nanocrystals. The data can be used for quantitatively for determining the chemical compositions of nanoparticles. EDS is mainly sensitive to heavy elements due to the fluorescence effect arising from Auger emission for light elements, while EELS is most adequate for light elements. Both EDS and EELS can be applied complementary to determine the chemical composition. The detection limit for EDS can be as high as 1%, and that for EELS can be as high as 5% depending on elements.

7.2. Near Edge Fine Structure and Electronic Structure. EELS is not only a powerful tool for microanalysis but can

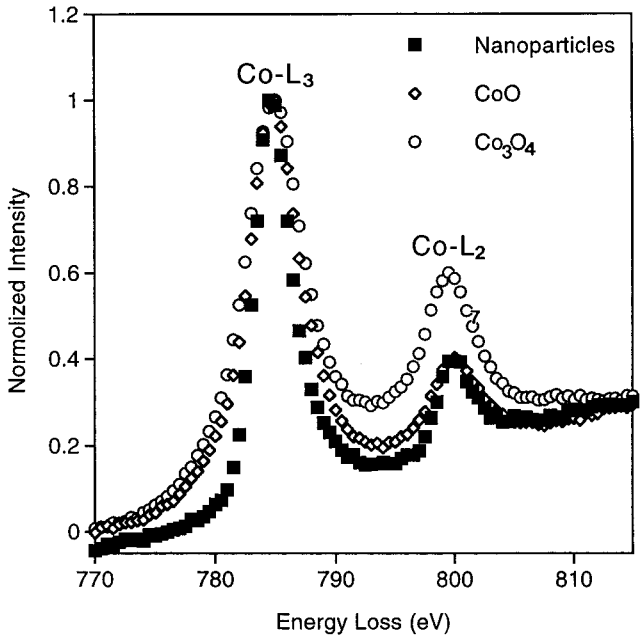

Figure 23. A comparison of EELS spectra of Co-$L_{2,3}$ ionization edges acquired from Co_3O_4 and CoO standard specimens and the synthesized nanocrystals, proving that the valence state of Co is 2+ in the newly prepared nanocrystals.

also provide electronic structural information. In the ionization edge observed in EELS, fine peaks present near the threshold represent the density of states in the conduction band. The intensities and energy position of the peaks are sensitive to the solid state structure of the material. The L ionization edges of transition metal and rare earth elements, for example, usually display sharp peaks at the near edge region, which are known as *white lines*. For transition metals with unoccupied 3d states, the transition of an electron from 2p state to 3d levels leads to the formation of white lines. The L_3 and L_2 lines are the transitions from $2p^{3/2}$ to $3d^{3/2}3d^{5/2}$ and from $2p^{1/2}$ to $3d^{3/2}$, respectively, and their intensities are related to the unoccupied states in the 3d bands.

Numerous EELS experiments have shown that a change in valence state of cations introduces a dramatic change in the ratio of the white lines, leading to the possibility of identifying the occupation number of 3d orbital using EELS. The most successful examples are Co and Mn oxides.[55−59] The oxidation states of Fe can also be determined, but the sensitivity is much lower.[60−62] The oxidation states of Ce and Pr have been determined in an orthophosphate material in which the constituents of Ce and Pr are on the order of 100 ppm.[63]

The determination of the crystal structure of nanoparticles is a challenge particularly when the particles are smaller than 5 nm. The intensity maxima observed in the X-ray or electron diffraction patterns of such small particles are broadened due to the crystal shape factor (see the diffraction pattern from the CoO nanocrystal inserted in Figure 16), greatly reducing the accuracy of structure refinement. On the other hand, the quality of the high-resolution TEM images of the particles is degraded because of the strong effect from the substrate. This difficulty arises in the study of CoO nanocrystals whose shape is dominated by tetrahedral of sizes smaller than 5 nm, but EELS can help to solve this problem. Figure 23 gives the EELS spectra acquired from the as-synthesized Co−O nanocrystals, and the bulk Co_3O_4 and CoO specimens. The spectrum of the nanoparticles fits very well with that of CoO, while that of Co_3O_4 is distinctly different, unambiguously proving the CoO structure of the nanocrystals.[44]

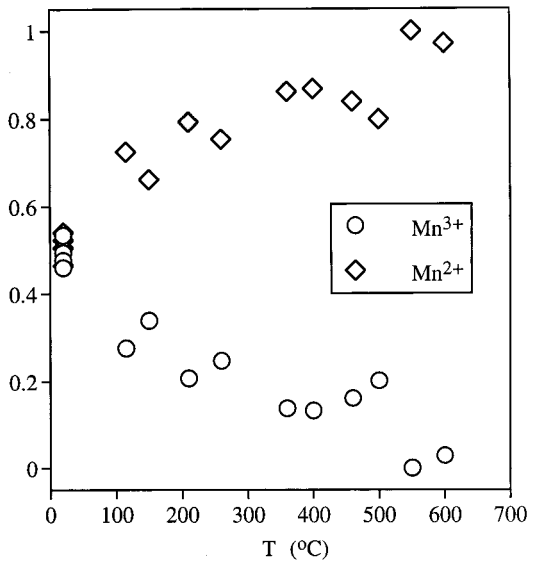

Figure 24. Fractions of the Mn^{2+} and Mn^{3+} ions in $MnFe_2O_4$ measured by quantitatively fitting the experimental EELS spectra with the standard spectra of the oxides containing Mn^{2+} and Mn^{3+} ions. Five repeated measurements at 25 °C are shown and give consistent result.

Analysis of the valence states of Mn has also been carried out for $MnFe_2O_4$ spaniel structured nanocrystals. The AB_2O_4 type of spaniel structure has two types of cation lattice sites: a tetrahedral site A^{2+} formed by four nearest-neighbor oxygen anions, and an octahedral B^{3+} site formed by six oxygen anions. In $MnFe_2O_4$, the percentage of the A sites occupied by Fe specifies the degree of valence inversion. For a general case, the ionic structure of $MnFe_2O_4$ is written as $(Mn^{2+}_{1-x}Fe^{2+}_{x})(Fe^{3+}_{1-y}Mn^{3+}_{y})O_4$, in which the A and B sites can be occupied by either Mn or Fe. An experimental measurement of the valence conversion of Mn in this material can provide concrete information on the distribution of Fe in the A and B sites, possibly leading to a better understanding on its magnetic property.[62] Shown in Figure 24 is the EELS measured fractions of the Mn^{2+} and Mn^{3+} ions in the $MnFe_2O_4$ specimen as a function of the in situ specimen temperature in TEM. The fraction was calculated by fitting the experimentally observed L_3 and L_2 EELS spectra by a linear summation of the spectra acquired from MnO and Mn_2O_3, and the coefficients for the linear combination give the percentages of the Mn ions of different valence states in the material. It is clear that the fractions of Mn^{2+} and Mn^{3+} ions at room temperature is 0.5:0.5, while a complete conversion into divalent Mn occurs at 600 °C. These data explicitly illustrate the evolution in the valence state of the Mn ions, leading to the temperature-dependent magnetic properties of $MnFe_2O_4$.

7.3. Chemical Mapping and Valence State Mapping. High spatial resolution mapping on the elemental distribution has vital importance in materials analysis. This can be carried in the scanning mode by collecting EDS/EELS signal at each scanning position of the beam.[63,64] A detailed data processing provides a distribution map of the elements. The spatial resolution is mostly determined by the size of the electron probe. In TEM, images can be formed by the electrons that have lost a specific energy in correspondence to an energy threshold of the atomic inner shell. This is the energy-filtered transmission electron microscopy (EF-TEM).[67,68] With consideration of the fact that the inner shell excitation of an atom occurs only when the impact parameter of an incident electron is less than 0.05 nm, this very localized scattering characteristic is the origin of mapping the distribution of the element that gives rise to the inner shell

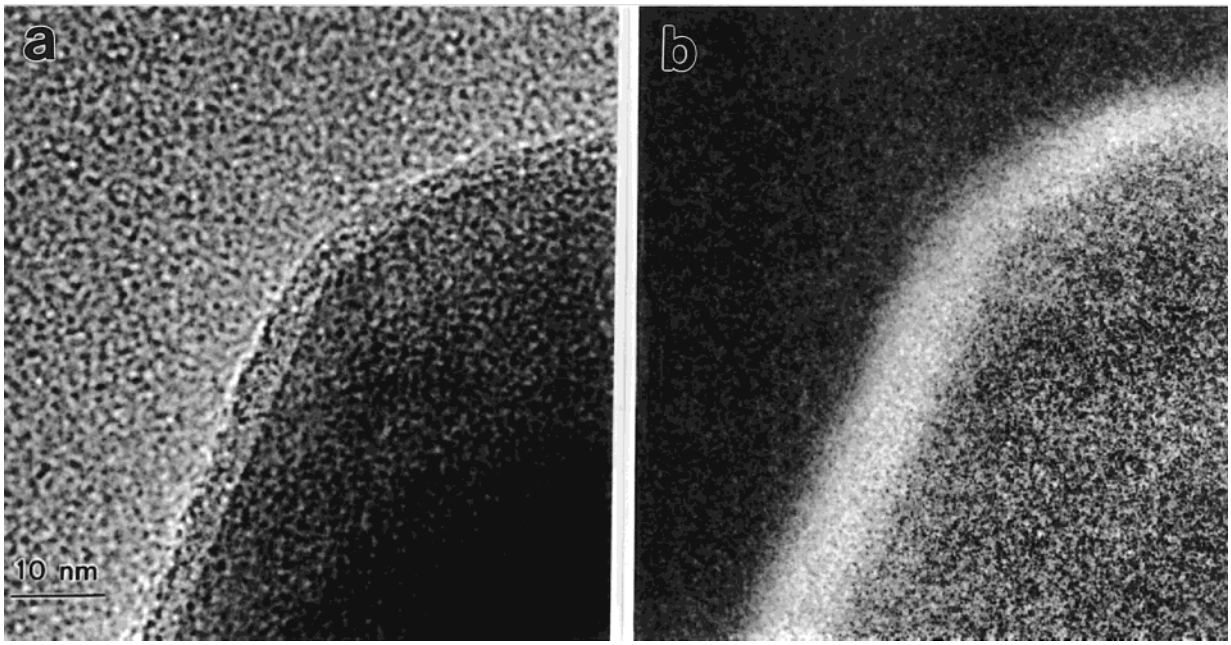

Figure 25. (a) Bright-field and (b) Si-L edge energy filtered TEM images of a TiO_2 particle coated with silica.

excitation. This technique has been applied to map the distribution of thiolates in the self-assembled Ag nanocrystals.[42] The result proves that the adsorbed molecules are distributed on the surfaces of the nanocrystals and they form interdigitative bundling that holds the nanocrystal together.

Figure 25a shows a bright-field TEM image recorded from a TiO_2 specimen coated with 1 at. % silica and embedded in epoxy. The amorphous layer of thickness 4 nm coated on the particle surface cannot be easily claimed as silica from this image. Using the Si-L edge, the energy-filtered image confirms that the layer is indeed silica (Figure 25b). The width of the silica layer in the Si-L edge filtered image is significantly wider than that in the bright field image. This is due to a deterioration in image resolution by chromatic aberration because of the 20 eV wide energy window.

We have illustrated the sensitivity of near edge fine structures to the valence states of transition metal elements. Energy-filtered imaging by selecting the electrons with an energy loss in correspondence to the near edge structure contains the spatial distribution of the valence states across the region. A typical example is the mapping of SP_2 and SP_3 bonds in diamond-like materials.[69,70] Using the images acquired from the white lines, an experimental approach has been demonstrated to map the valence state distributions of Mn and Co using the energy-filtered TEM.[69] Figure 23 clearly shows the strong dependence of the relative intensities of the Co-L_3 and Co-L_2 white lines on the valence state of cobalt. In EF-TEM, if an energy window of 12 eV in width is positioned at the L_3 and the L_2 white lines, the energy filtered images using the Co-L_3 and Co-L_2 lines can be obtained after subtraction of background. The ratio L_3/L_2 image gives the distribution of valence states across the specimen.[71]

Figure 26 shows a group of energy-filtered TEM images from a triple point in the $CoO-Co_3O_4$ specimen. The energy-filtered images using the L_3 and L_2 lines and the post-L_2 line region (parts a−c of Figure 26) show a distinct difference in contrast distribution due to a difference in the relative white line intensities. From these three images, the L_3/L_2 is calculated after subtracting the contribution from the continuous energy loss region that is due to single atom scattering, and the image clearly displays the distribution of cobalt oxides having different valence states (Figure 26e), where the diffraction contrast disappears. The region with lower oxidation state (Co^{2+}) shows stronger contrast, and the ones with high oxidation states show weaker contrast. The O/Co image was calculated from the images recorded from the O-K edge and the $L_3 + L_2$ white lines for an energy window width of $\Delta = 24$ eV. Although the energy-filtered O-K edge image exhibits some diffraction contrast and the thickness effect, the O/Co compositional ratio image greatly reduces the effect. The high intensity region in the O/Co image indicates the relative high local concentration in oxygen (e.g., higher Co oxidation states), the low intensity region contains relatively less oxygen (e.g., lower Co valence state), entirely consistent with the information provided by the L_3/L_2 image. A spatial resolution of ~2 nm has been achieved. This is remarkable in comparison to any existing techniques.

8. Holography Imaging of Charged and Magnetic Nanocrystals

HRTEM is powerful in resolving the atomic scale microstructure of nanocrystals, but it is insensitive to the electrostatic charging or magnetic domain of a nanocrystal because the electron phase caused by the electromagnetic phenomena is "lost" in the recording of the image. The phase image can provide the distribution of electrostatic field around a charged particle as well as the thickness-projected potential image of a nanocrystal. The former can be used to extract the charge distribution in the particle,[72] and the latter is useful to determine whether the particle contains a hard core or an empty cavity.[73] Mapping the electron phase around a magnetic particle can reveal the magnetic domain structure in a nanocrystal.[74,75] The mapping of electron phase is based on an electron holography technique.

The principle of electron holography was first introduced by Gabor.[76] Holography is based on the interference and diffraction properties of waves, thereby producing a true image of an object (including amplitude and phase) without any distortion of the lenses. The development of high-brightness, high-coherence electron sources has made it possible to obtain holograms using electron waves in TEM.[77−79] The key application of electron holography is studying magnetic materials. A key step in

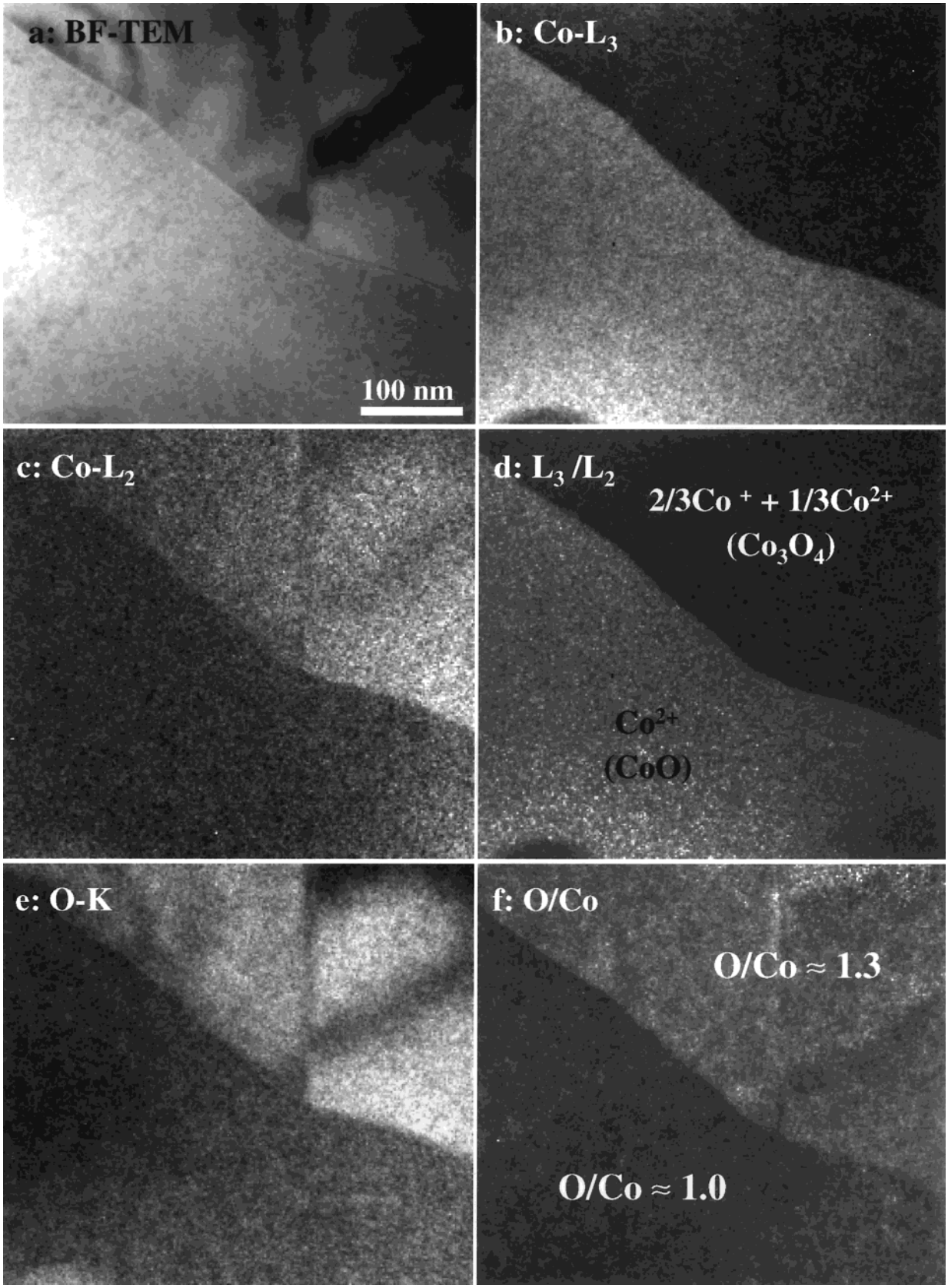

Figure 26. A group of images recorded from the same specimen region using signals of (a) the Bright-field, (b) the Co-L_3 edge, and (c) the Co-L_2 edge. (d) The processed L_3/L_2 image, displaying the distribution of the valence states. (e) Oxygen map acquired by the O-K edge. (f) The atomic concentration ratio image of O/Co. The continuous background contributed from the single atom scattering has been removed from the displayed Co-L_3 and Co-L_2 images. The O/Co image is normalized in reference to the standard composition of CoO for the low portion of the image in order to eliminate the strong influence on the ionization cross section from the white lines. Each raw image was acquired with an energy window width of $\Delta = 12$ eV except for O-K at $\Delta = 24$ eV.

observation of magnetic flux lines is to create a magnetic-field-free zone in which the specimen to be examined is placed. This can be achieved either by switching off the objective lens or by using a Lorentz objective lens. In the former, the experiments

can be performed using a conventional TEM equipped with an FEG at the expense of image magnification, which is usually reduced by 50−80 times. The image resolution is also greatly reduced due to the aberration effect of the intermediate lenses. Thus, the technique can only be applied to image magnetic domains of large sizes.

9. Summary

Controlling the shape of nanocrystals is the-state-of-the-art in nanophase materials research. The shape-controlled nanocrystals have many prospects that are likely to impact the fields of catalysis, self-assembly, and nanodevices. An important technique for characterizing the shape-controlled nanocrystals is transmission electron microscopy. The objective of this article is to introduce TEM techniques for characterization of the shape-controlled nanocrystals. The most important application of TEM is to define the shape of nanocrystals. This type of imaging capability is well received by the physical chemistry community.

In additional to high-resolution lattice imaging, TEM is powerful in identifying and quantifying the chemical and electronic structure of nanomaterials. High spatial resolution analysis is vitally important for solving many of the practical problems of nanomaterials. Spectroscopy analysis of the solid state effects and the valence states mapping are new directions of quantitative microscopy. Further exploration in the fine structures in EELS is likely to reveal rich information about bonding in nanocrystals. In situ TEM is anticipated to be important for characterizing and measuring the properties of individual nanostructures, from which the structure−property relationship can be clearly registered to a specific nanoparticle/structure. This is a new growing field of nanomeasurements.

Acknowledgment. Thanks to my collaborators, M. A. El-Sayed, W. A. de Heer, R. L. Whetten, S. A. Harfenist, Jin Song Yin, Z. J. Zhang, P. Poncharal, T. Ahmadi, M. Mohamed, S. Link, Janet Petroski, and T. C. Green, for their contributions to the work covered in this review article. This research was sponsored by NSF Grants CHE-9727633 and DMR-9733160.

References and Notes

(1) Buffat, Ph.; Borel, J.-P. *Phys. Rev. A* **1976**, *13*, 2287.
(2) Schmidt, M.; Kusche, R.; von Issendorff, B.; Haberland, H. *Nature* **1998**, *393*, 238.
(3) Goldstein, A. N.; Echer, C. M.; Alivisatos, A. P. *Science* **1992**, *256*, 1425.
(4) de Heer, W. A. *Rev. Mod. Phys.* **1993**, *65*, 611.
(5) Alivisatos, A. P. *Science* **1996**, *271*, 933.
(6) Mohamed, M.; Wang, Z. L.; El-Sayed, M. A. *J. Phys. Chem. B*, in press.
(7) Wang, Z. L.; Petroski, J.; Green, T.; El-Sayed, M. A. *J. Phys. Chem. B* **1998**, *102*, 6145.
(8) Cleveland, C.; Luedtke, W. D.; Landman, U. *Phys. Rev. Lett.* **1998**, *81*, 2036.
(9) Wang, Z. L., Ed. *Characterization of Nanophase Materials*; Wiley-VCH: New York, 2000.
(10) Williams, D. B.; Carter, C. B. *Transmission Electron Microscopy*; Plenum Press: New York, 1996.
(11) Wang, Z. L.; Kang, Z. C. *Functional and Smart Materials − Structural Evolution and Structure Analysis*; Plenum Press: New York, 1998; Chapter 6.
(12) Egerton, R. F. *Electron Energy-Loss Spectroscopy in the Electron Microscope*, 2nd ed.; Plenum Press: New York, 1996.
(13) Frank, S.; Poncharal, P.; Wang, Z. L.; de Heer, W. A. *Science* **1998**, *280*, 1744. Poncharal, P.; Frank, S.; Wang, Z. L.; de Heer, W. A. *Proceeding of the International Conference on Small Clusters*, in press.
(14) Ahmadi, T. S.; Wang, Z. L.; Green, T. C.; Henglein, A.; El-Sayed, M. A. *Science* **1996**, *28*, 1924.
(15) Hirsch, P. B.; Howie, A.; Nicholson, R. B.; Pashley, D. W.; Whelan, M. J. *Electron Microscopy of Thin Crystals*; Roberts E. Krieger Publishing Company: New York, 1977.
(16) Scherzer, O. *J. Appl. Phys.* **1949**, *20*, 20.
(17) Wang, Z. L. *Elastic and Inelastic Scattering in Electron Diffraction and Imaging*; Plenum Press: New York, 1995; Chapters 2−5.
(18) Cowley, J. M.; Moodie, A. F. *Acta Crystallogr.* **1957**, *10*, 609.
(19) Ascencio, J. A.; Gutiérrez-Wing, C.; Espinosa, M. E.; Marin, M.; Tehuacanero, S.; Zorrilla, C.; José-Yacamán, M. *Surf. Sci.* **1998**, *396*, 349.
(20) Smith D. J.; Marks, L. D. *Philos. Mag. A* **1981**, *44*, 735.
(21) Rampino, L. D.; Nord, F. F. *J. Am. Chem. Soc.* **1942**, *63*, 2745.
(22) Henglein, A.; Ershov, B. G.; Marlow, M. *J. Phys. Chem.* **1995**, *99*, 14129.
(23) Wang, Z. L.; Ahmadi, T. S.; El-Sayed, M. A. *Surf. Sci.* **1996**, *380*, 302.
(24) Ino, S. *J. Phys. Soc. Jpn.* **1966**, *21*, 346.
(25) Allpress, J. G.; Sanders, J. V. *Surf. Sci.* **1967**, *7*, 1.
(26) Marks, L. D. *Rep. Prog. Phys.* **1994**, *57*, 603 and references therein.
(27) Yang, C. Y. *J. Cryst. Growth* **1979**, *47*, 274; **1979**, *47*, 283.
(28) Buffat, P.-A.; Flüeli, M.; Spycher, R.; Stadelmann, P.; Borel, J.-P. *Faraday Discuss.* **1991**, *92*, 173.
(29) Cleveland, C. L.; Landman, U.; Schaaff, T. G.; Shafigullin, M. N.; Stephens, P. W.; Whetten, R. L. *Phys. Rev. Lett.* **1997**, *79*, 1873.
(30) Ikarashi, N.; Kobayashi, K.; Koike, H.; Hasegawa, H.; Yagi, K. *Ultramicroscopy* **1988**, *26*, 195.
(31) Petroski, J. M.; Wang, Z. L.; Green, T. C.; El-Sayed, M. A. *J. Phys. Chem. B* **1998**, *10*, 3316.
(32) Yu, Y.-Y.; Chang, S.-S.; Lee, C.-L.; Wang, C. R. *J. Phys. Chem. B* **1997**, *101*, 6661.
(33) Iijima, S.; Ichihashi, T. *Phys. Rev. Lett.* **1986**, *56*, 616.
(34) Smith, D. J.; Petford-Long, A. K.; Wallenberg, L. R.; Bovin, J.-O. *Science* **1986**, *233*, 872.
(35) Whetten, R. L.; Khoury, J. T.; Alvarez, M. M.; Murthy, S.; Vezmar, I.; Wang, Z. L.; Cleveland, C. C.; Luedtke, W. D.; Landman, U. *Adv. Mater.* **1996**, *8*, 428.
(36) Wang, Z. L. *Adv. Mater.* **1998**, *10*, 13.
(37) Motte, L.; Billoudet, F.; Lacaze, E.; Douin, J.; Pileni, M.-P. *J. Phys. Chem B* **1997**, *101*, 138.
(38) Andres, R. P.; Bein, T.; Dorogi, M.; Feng, S.; Henderson, J. I.; Kubiak, C. P.; Mahoney, W.; Osifchin, R. G.; Reifenberger, R. *Science* **1996**, *272*, 1323.
(39) Murray, C. B.; Kagan, C. R.; Bawendi, M. G. *Science* **1995**, *270*, 1335.
(40) Collier, C. P.; Saykally, R. J.; Shiang, J. J.; Henrichs, S. E.; Heath, J. R. *Science* **1997**, *277*, 1978.
(41) Harfenist, S. A.; Wang, Z. L.; Alvarez, M. M.; Vezmar, I.; Whetten, R. L. *J. Phys. Chem.* **1996**, *100*, 13904.
(42) Wang, Z. L.; Harfenist, S. A.; Whetten, R. L.; Bentley, J.; Evans, N. D. *J. Phys. Chem. B* **1998**, *102*, 3068.
(43) Wang, Z. L.; Harfenist, S. A.; Vezmar, I.; Whetten, R. L.; Bentley, J.; Evans, N. D. *Adv. Mater.* **1998**, *10*, 808.
(44) Yin, J. S.; Wang, Z. L. *Phys. Rev. Lett.* **1997**, *79*, 2570.
(45) Harfenist, S. A.; Wang, Z. L.; Alvarez, M. M.; Vezmar, I.; Whetten, R. L. *Adv. Mater.* **1997**, *9*, 817.
(46) Bentzon, M. D.; Thölen, A. *Ultramicroscopy* **1991**, *38*, 105.
(47) Ahmadi, T. S.; Wang, Z. L.; Green, T. C.; Henglein, A.; El-Sayed, M. A. *Chem. Mater.* **1996**, *8*, 1161.
(48) Link, S.; Burda, C.; Mohamed, M. B.; El-Sayed, M. A. *J. Phys. Chem. B* **1999**, *103*, 1165.
(49) Mohamed, M. B.; Ismail, K. Z.; Link, S.; El-Sayed, M. A. *J. Phys. Chem. B* **1999**, *102*, 9370
(50) Harfenist, S. A.; Wang, Z. L. *J. Phys. Chem. B* **1999**, *103*, 4342.
(51) Yin, J. S.; Wang, Z. L. *J. Phys. Chem.* **1997**, *101*, 8979.
(52) Poncharal, P.; Wang, Z. L.; Ugarte, D.; de Heer, W. A. *Science* **1999**, *283*, 1513.
(53) Frank, S.; Poncharal, P.; Wang, Z. L.; de Heer, W. A. *Science* **1998**, *280*, 1744.
(54) Goldstein, J. I.; Newbury, D. E.; Echlin, P.; Joy, D. C.; Romig, A. D.; Lyman, C. E.; Fiori, C.; Lifshin, E. *Scanning Electron Microscopy and X-ray Microanalysis, a text for biologists, materials scientists and geologists*; Plenum Press: New York, 1992.
(55) Kurata, H.; Colliex, C. *Phys. Rev. B* **1993**, *48*, 2102.
(56) Mansot, J. L.; Leone, P.; Euzen, P.; Palvadeau, P. *Microsc. Microanal. Microstruct.* **1994**, *5*, 79.
(57) Wang, Z. L.; Yin, J. S.; Zhang, J. Z.; Mo, W. D. *J. Phys. Chem. B* **1997**, *101*, 6793.
(58) Wang, Z. L.; Yin, J. S.; Jiang, Y. D.; Zhang, J. *Appl. Phys. Lett.* **1997**, *70*, 3362.
(59) Wang, Z. L.; Yin, J. S. *Philos. Mag. B* **1998**, *77*, 49.
(60) Colliex, C.; Manoubi, T.; Ortiz, C. *Phys. Rev. B* **1991**, *44*, 11402.
(61) Lloyd, S. J.; Botton, G. A.; Stobbs, W. M. *J. Microsc.* **1995**, *180*, 288.
(62) Yuan, J.; Gu, E.; Gester, M.; Bland, J. A. C.; Brown, L. M. *J. Appl. Phys.* **1994**, *75*, 6501.
(63) Fortner, J. A.; Buck, E. C. *Appl. Phys. Lett.* **1996**, *68*, 3817.
(64) Zhang, Z. J.; Wang, Z. L.; Chakoumakos, B. C.; Yin, J. S. *J. Am. Chem. Soc.* **1998**, *120*, 1800.

(65) Craven, A. J.; Colliex, C. *J. Microsc. Spectrosc. Electron* **1977**, *2*, 511.

(66) Leapman, R. D.; Hunt, J. A. *Microscopy: The Key Research Tool*; The Electron Microscopy Society of America, 1992; Vol. 22, p 39.

(67) Reimer, L., Ed. *Energy Filtering Transmission Electron Microscopy*; Springer Series in Optical Science; Springer-Verlag: New York, 1995.

(68) Wang, Z. L.; Shapiro, A. J. *Ultramicroscopy* **1995**, *60*, 115.

(69) Mayer, J.; Plitzko, J. M. *J. Microsc.* **1996**, *183*, 2.

(70) Batson, P. E.; Browning N. D.; Muller, D. A. *MSA Bull.* **1994**, *24*, 371.

(71) Wang, Z. L.; Bentley, J.; Evans, N. D. *J. Phys. Chem. B* **1999**, *103*, 751.

(72) Frost, B. G.; Allard, L. F.; Volkl, E.; Joy, D. C. In *Electron Holography*; Tonomura, A., Allard, L. F., Pozzi, G., Joy, D. C., Ono, Y. A., Eds.; Elsevier Science: New York, 1995; p 169.

(73) Datye, A. K.; Kalakkad, D. S.; Vöikl, E.; Allard, L. F. In *Electron Holography*; Tonomura, A., Allard, L. F., Pozzi, G., Joy, D. C., Ono, Y. A., Eds.; Elsevier Science: New York, 1995; p 199.

(74) Mankos, M.; Cowley, J. M.; Scheinfein, M. R. *Mater. Res. Soc. Bull.* **1995**, *20*, 45.

(75) Hirayama, T.; Chen, J.; Ru, Q.; Ishizuka, K.; Tanji, T.; Tonomura, A. In *Electron Holography*; Tonomura, A., Allard, L. F., Pozzi, G., Joy, D. C., Ono, Y. A., Eds.; Elsevier Science: New York, 1995; p 145.

(76) Gabor, D. *Proc. R. Soc. London A* **1949**, *197*, 454.

(77) Tonomura, A. *Electron Holography*; Springer-Verlag: New York, 1993.

(78) Lichte, H. *Adv. Opt. Electron Microsc.* **1991**, *12*, 25.

(79) Tonomura, A., Allard, L. F., Pozzi, G., Joy, D. C., Ono, Y. A., Eds.; *Electron Holography*; Elsevier Science: New York, 1995.